End-to-end simulations to optimize imaging spectroscopy mission requirements for seven scientific applications

Xavier Briottet, Karine Adeline, T. Bajjouk, V. Carrere, Malik Chami, Yohann Constans, Yevgeny Derimian, Alice Dupiau, Marie Dumont, Stéphanie Doz, et al.

To cite this version:

Xavier Briottet, Karine Adeline, T. Bajjouk, V. Carrere, Malik Chami, et al.. End-to-end simulations to optimize imaging spectroscopy mission requirements for seven scientific applications. 2023. hal-04500503v1

HAL Id: hal-04500503
https://hal.science/hal-04500503v1

Preprint submitted on 30 Nov 2023 (v1), last revised 13 Mar 2024 (v2)

Date: Wednesday, November 15, 2023

Title: End-to-end simulations to optimize imaging spectroscopy mission requirements for seven scientific applications

Authors: Briottet X.[1*], Adeline K.[1], Bajjouk T.[2], Carrère V.[3], Chami M.[4], Constans Y.[1], Derimian Y.[5], Dupiau A.[1,6], Dumont M.[7], Doz S.[1], Fabre S.[1], Foucher P. Y.[1], Herbin H.[5], Jacquemoud S.[6], Lang M.[8], Le Bris A.[9], Litvinov P.[16], Loyer S.[10], Marion R[11], Minghelli A.[12], Miraglio T.[1], Sheeren D.[8], Szymanski B.[13], Romand F.[15], Desjardins C.[14], Rodat D.[14], Cheul B.[14]

[1] Université de Toulouse, ONERA DOTA, Toulouse, France, xavier.briottet@onera.fr, karine.adeline@onera.fr, sophie.fabre@onera.fr, yohann.constans@onera.fr, stephanie.doz@onera.fr, pierre-yves.foucher@onera.fr, thomas.miraglio@gmail.com

[2] Ifremer, DYNECO, LEBCO, Plouzané, France, touria.bajjouk@ifremer.fr

[3] Nantes Université, Laboratoire de Planétologie et Géosciences, UMR 6112, Nantes, France, veronique.carrere@univ-nantes.fr

[4] Université Côte d'Azur, Observatoire de la Côte d'Azur, CNRS, Sorbonne Université, Laboratoire Lagrange, Nice, France, malik.chami@upmc.fr

[5] Université Lille, CNRS, UMR 8518, LOA, France, herve.herbin@univ-lille.fr, yevgeny.derimian@univ-lille.fr

[6] Université Paris Cité, Institut de physique du globe de Paris, CNRS, Paris, France, jacquemoud@ipgp.fr

[7] Université Grenoble Alpes, Université de Toulouse, Météo-France, CNRS, CNRM, Centre d'Etudes de la Neige, Grenoble, France, marie.dumont@meteo.fr

[8] Université de Toulouse, INRAE, UMR DYNAFOR; Castanet-Tolosane, France, marc.lang@toulouse-inp.fr, david.sheeren@ensat.fr

[9] Université Gustave Eiffel, LASTIG, ENSG, IGN, Saint-Mandé, France, arnaud.le-bris@ign.fr

[10] SHOM, Brest, France, sophie.loyer@shom.fr

[11] CEA/DAM/DIF, Arpajon, France, rodolphe.marion@cea.fr

[12] Université de Toulon, CNRS, SeaTech, LIS laboratory, UMR 7020, Toulon, France, audrey.minghelli@univ-tln.fr

[13] DGA, Paris, France, benjamin.szymanski@intradef.gouv.fr

[14] CNES, Toulouse, France, camille.desjardins@cnes.fr, damien.rodat@cnes.fr, benoit.cheul@cnes.fr

[15] ACRI-ST, Sophia-Antipolis, France, frederic.romand@acri-st.fr

[16] GRASP SAS, Villeneuve d'Ascq, France, pavel.litvinov@grasp-sas.com

[*] Corresponding author: xavier.briottet@onera.fr

Keywords: imaging spectroscopy, signal-to-noise ratio, spectral sampling, image quality, mineralogy, soil moisture content, tree species, leaf functional traits, bottom classification, shallow water, bathymetry, seabed, urban land cover, plume, aerosols, methane, cryosphere, water vapor, aerosols

Highlights:

- Assess the impact of instrumental design on various end-user hyperspectral applications,

- Evaluation of the main sources of error, namely the signal-to-noise ratio (SNR), the radiometric calibration and the spectral sampling strategy,
- Analysis of sensibility to the instrumental configurations for each application.

Journal: ISPRS Open Journal of Photogrammetry and Remote Sensing

● Abstract

CNES is currently carrying out a Phase A study to assess the feasibility of a future hyperspectral imaging sensor (10 m spatial resolution) combined with a panchromatic camera (2.5 m spatial resolution). This mission focuses on both high spatial and spectral resolution requirements, as inherited from previous French studies such as HYPEX, HYPXIM, and BIODIVERSITY. To meet user requirements, cost, and instrument compactness constraints, CNES asked the French hyperspectral Mission Advisory Group (MAG), representing a broad French scientific community, to provide recommendations on spectral sampling, particularly in the Short Wave InfraRed (SWIR) for various applications.

This paper presents the tests carried out with the aim of defining the optimal spectral sampling and spectral resolution in the SWIR domain for quantitative estimation of physical variables and classification purposes. The targeted applications are geosciences (mineralogy, soil moisture content), forestry (tree species classification, leaf functional traits), coastal and inland waters (bathymetry, water column, bottom classification in shallow water, coastal habitat classification), urban areas (land cover), industrial plumes (aerosols, methane and carbon dioxide), cryosphere (specific surface area, equivalent black carbon concentration), and atmosphere (water vapor, carbon dioxide and aerosols). All the products simulated in this exercise used the same CNES end-to-end processing chain, with realistic instrument parameters, enabling easy comparison between applications. 648 simulations were carried out with different spectral strategies, radiometric calibration performances and signal-to-noise Ratios (SNR): 24 instrument configurations × 25 datasets (22 images + 3 spectral libraries).

The results show that a 16/20 nm spectral sampling in the SWIR domain is sufficient for most applications. However, 10 nm spectral sampling is recommended for applications based on specific absorption bands such as mineralogy, industrial plumes or atmospheric gases. In addition, a slight performance loss is generally observed when radiometric calibration accuracy decreases, with a few exceptions in bathymetry and in the cryosphere for which the observed performance is severely degraded. Finally, most applications can be achieved with the lowest SNR, with the exception of bathymetry, shallow water classification, as well as carbon dioxide and methane estimation, which require the higher SNR level tested. On the basis of these results, CNES is currently evaluating the best compromise for designing the future hyperspectral sensor to meet the objectives of priority applications.

1. Introduction

Imaging spectroscopy (IS) is now recognized as a powerful tool for satellite-based Earth observation. Several sun-synchronous space missions such as Gaofen 5 (Liu et al., 2019), PRISMA (Meini et al., 2015) or EnMap (Guanter et al., 2015) are already operational (Qian, 2021). They offer global coverage with a revisit time from 4 to 29 days. All these sensors have a ground sampling distance (GSD) of 30 m which reduces the range of applications due to the presence of mixed pixels in heterogeneous scenes (Zhao et al., 2014; Transon et al., 2018). Spatial resolution is considered the « Achille heel » for the recovery of fine-scale surface parameters. Other authors have mentioned these limitations for crop disease detection (Dutta et al., 2006; White et al., 2007), forest functional traits estimation (Miraglio et al., 2022), urban area classification (Cavalli et al., 2008; Heldens et al., 2011), clay mineral mapping (Gomez et al., 2015), characterization of acid mine drainage (Davies and Calvin, 2017), monitoring of industrial gas plumes (methane, carbon dioxyde), smoke (Nesme et al., 2021; Deschamps et al., 2013), or early detection of coral bleaching (Yamano and Tamura, 2004). Ustin and Middleton (2021) reported that a 10 m GSD is justified to improve the mapping capabilities of crops, minerals, snow/ice, water resources, vegetation type and condition.

There is therefore a real need to complement existing IS sensors with a new sensor with better spatial resolution. A number of IS missions are currently under study, such as SHALOM (Feingersh et Ben-Dor, 2016) and PRISMA-NG (Ansalone et al., 2021). For many years, French researchers supported by CNES/DGA have been working on specifications of a new 10 m GSD IS sensor under several names: HYPXIM (Briottet et al., 2011; Carrère et al., 2013), HYPEX-2 (Briottet et al., 2017) and BIODIVERSITY (Briottet et al., 2022). A phase A, led by CNES was completed in mid-2022 with the aim of proposing an instrument combining hyperspectral imaging (10 m GSD, spectral range 0.45–2.40 μm, 10 km swath) with panchromatic imagery (2.5 m GSD) with a revisit time of 5 days. One of the aims of this study was to define the optimum signal-to-noise ratio (SNR), radiometric image quality and spectral sampling for different applications, within the constraint of instrument compactness: geosciences, forestry, coastal and inland waters, urban areas, industrial plumes, cryosphere, and atmosphere. All these applications have been selected because they require high spatial resolution, on the order of 10 m, and correspond to the themes identified by Taramelli et al. (2020). The aim of this work is therefore to present the results of a cross-analysis of these scientific fields, which will help consolidate the mission requirements and the payload design.

After describing the input data in §2, the end-to-end simulator for calculating radiance at the top of the atmosphere is presented in §3, along with the insertion of specific sensor characteristics (spectral strategy, SNR, radiometric calibration accuracy), the choice of surface reflectance and the methods used to extract the relevant parameters for each application. The results are presented in §4, followed by a discussion in §5 and a conclusion in §6.

2. Materials

Two types of input data were used to cover these seven scientific domains: reflectance spectra measured in the laboratory or simulated using dedicated models, presented in §2.1, and hyperspectral images (§2.2).

2.1. Laboratory, field and simulated spectra

The use of laboratory measured spectra concerns applications in mineralogy and soil moisture content (SMC) estimation (geosciences), while the use of simulated spectra concerns applications in leaf functional traits estimation (vegetation), spectral surface area (SSA) and equivalent black carbon (eBC) estimation (cryosphere), and atmospheric aerosol and gas estimation (atmosphere).

For mineralogy estimation, 38 reflectance spectra of 16 minerals of interest (clays, carbonates, sulphates, rare earth elements (REE), oxy-hydroxides, etc.) with a wide range of chemical composition and grain size were selected from the United States Geological Survey (USGS) Spectral Library (https://crustal.usgs.gov/speclab/). The results presented here are limited to the 11 most typical minerals whose spectral characteristics are given in Table 1**.**

Table 1. Diagnostic absorption characteristics of 11 representative minerals. Bastnaesite, monazite, and xenotime have specific absorption peaks in the visible and near-infrared (VNIR) due to varying proportions of rare earth elements: only the four main absorption peaks are shown.

Mineral	USGS Reference	Wavelength positions of diagnostic absorption features
Gypsum	Gypsum_HS333.3B	~1.75 µm; secondary absorption ~2.21 µm
Calcite	Calcite_WS272	~2.34 µm; secondary absorption ~2.16 µm
Kaolinite	Kaolinite_CM9	Doublet ~2.16 µm and ~2.21 µm
Alunite	HS295-3B	~1.76 µm, ~2.16 µm; secondary absorption ~2.32 µm
Goethite	Goethite_GDS134	~0.66 µm, ~0.91 µm; secondary absorption ~0.50 µm
Hematite	Hematite_HS45.3	~0.86 µm; secondary absorption ~0.66 µm
Jarosite	Jarosite_GDS635_Na_Cyprus	~0.43, ~0.92, 2.21 and 2.27 µm
Montmorillonite	Montmorillonite_SAz-1	~2.22 µm
Bastnaesite	Bastnaesite_REE_WS320	~ 0.58 ,0.74, 0.80 and 0.86 µm
Monazite	Monazite_REE_GDS947_Calif	~ 0.58, 0.75, 0.80 and 0.87 µm
Xenotime	Xenotime_GDS966_Iveland_REE	~ 0.66, 0.75, 0.81 and 0.91 µm

For coastal habitat classification, a library of field spectra was acquired using an ASD FieldSpec 4 Hi-Res spectroradiometer, which covers the wavelength range from 350 and 2500 nm with spectral resolution ranging from 3 nm (VIS-NIR) to 8 nm (SWIR). The spectra recorded over 2151 bands were calibrated using a Spectralon to provide reflectance factor measurements. Three to five spectra were recorded on each target to account for intra-target variability. These targets have different benthic characteristics: vegetation types (green, red, brown algae and microphytobenthos) and substrate types (mud, sand, shells and rocks), *Sabellaria alveolata* bioconstructions, oyster reefs, etc. This spectral library will enable us to access the potential of the SWIR for discriminating intertidal benthic feature, given that we have no images in the coastal zone in this wavelength range.

For SMC, reflectance spectra of 32 soils measured for different gravimetric water contents ranging from 5% to 85% were extracted from the Les08 database (Lesaignoux et al., 2013; Figure 1) used to validate the Multilayer rAdiative tRansfer Model of soIl reflectance (MARMIT) model (Bablet et al., 2018, Dupiau et al., 2022).

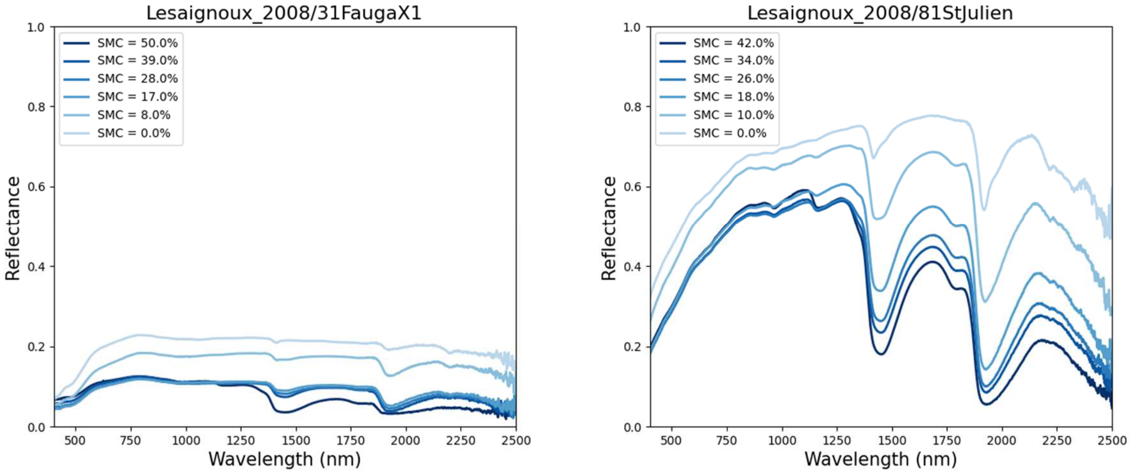

Figure 1. Reflectance spectra of two soil samples (81StJulien and 31FaugaX1) extracted from the Les08 database (Lesaignoux et al., 2013). https://pss-gitlab.math.univ-paris-diderot.fr/marmit/marmit

For the estimation of leaf functional traits, a spectral database was generated using the DART ray-tracing model (Gastellu-Etchegorry et al., 2012) coupled to the PROSPECT leaf radiative transfer model (Jacquemoud et al., 1996) with the input variables described in Table 2. The objective is to simulate top of canopy reflectance images similar to those acquired by an airborne hyperspectral sensor (see Miraglio et al., 2022).

Table 2. Range of variation in biochemical and physical properties of trees. FVC: fractional vegetation cover, LAD: leaf angle distribution, ALA: average leaf angle, LAI: leaf area index, Cab: chlorophyll content, Car: carotenoid content, EWT: equivalent water thickness, and N: leaf structure parameter in PROSPECT.

Canopy parameter	**Value and range**
FVC (%)	30, 50, 70, 90
LAD (°)	Ellipsoidal
ALA (°)	55-65
LAI (m^2/m^2)	1-4
Cab ($\mu g/cm^2$)	5 - 70
Car ($\mu g/cm^2$)	4 - 20
EWT (g/cm^2)	0.001 – 0.025
LMA (g/cm^2)	0.001 – 0.025
N	1.5 – 2.1

To estimate the specific surface area (SSA) and the equivalent black carbon (eBC) concentration, snow reflectance spectra were simulated with the Two-streAm Radiative TransfEr in Snow model (TARTES, Libois et al., 2013) with the input parameters detailed in

Table 3. SSA and eBC values were determined using *in situ* hyperspectral measurements (Libois et al., 2013; Picard et al., 2016; Dumont et al., 2017; Tuzet et al., 2019, 2020).

Table 3. Definition of the variation ranges of the inputs for the TARTES simulations.

Variable	Range
Spectral range	350-3000 nm at 1 nm resolution
Specific surface area (SSA)	3-100 kg m^{-2}
Sun zenith angle	0-80° by 10° step
Dust	11 values between 0 and 500 10^{-6} g g^{-1}
Equivalent black carbon (eBC) concentration	11 values between 0 and 300 10^{-9} g g^{-1}

To estimate the composition of the gaseous atmosphere (water vapor, carbon dioxide), performance is assessed on the basis of a standard mid-latitude summer atmosphere, with a CO_2 concentration of 400 ppm. The observation is at nadir and the solar zenith angle is 20°, while the ground reflectance corresponds to a bright desert-like surface.

For atmospheric aerosols, synthetic TOA radiances were generated using the Generalized Retrieval of Aerosol and Surface Properties (GRASP, Dubovik et al. 2021) algorithm for a fixed geometry corresponding to a scattering angle of 150° and selected nominal wavelengths in the atmospheric windows (419, 441, 492, 546, 669, 770, 865, 2312 nm). Only a subset of wavelengths was selected, as the spectral characteristics of aerosols vary little in the solar domain. A mixture of two aerosol types with different size distributions, chemical compositions and shapes was used for the simulations: a fine mode for pollution particles and a coarse mode for desert dust. The influence of gases is negligible in this study, as the spectral bands were selected outside the main gas absorption peaks. The top of atmosphere reflectance ranged from 0.09 to 0.11 at 419 nm and around 0.01 at 2190 nm, representing different aerosol concentrations over a dark surface (water). Only one scenario is presented here, corresponding to a constant SNR of 200 in the 400-550 nm spectral range and 100 in the 600-2400 nm spectral range.

2.2. Airborne hyperspectral imaging

Images were acquired by airborne sensors with different spectral resolutions: NEO-HySpex (4-7 nm, https://www.neo.no/), NEO-ODIN (3-6 nm, https://www.neo.no/), AVIRIS-C (10 nm, https://aviris.jpl.nasa.gov/), and AVIRIS-NG (3.7 nm, https://aviris.jpl.nasa.gov/). They all cover the 0.4-2.5 µm spectral range. Table 4 lists the images and variables of interest for each scientific field.

Table 4. IS images used in this study, with θ_S sun zenith angle applied in subsequent simulations and all the images are acquired at nadir.

Scientific domain	Acquisition date	Location	Sensor characteristics	Applications: Variable of interest
Geosciences	Sept. 2019 $\theta_S = 50.5^\circ$	Cherves-Richemont, France	HySpex: GSD$_{VNIR}$ = 0.5 m GSD$_{SWIR}$ = 1 m	Mineralogy: gypsum, calcite
	Sept. 2019 $\theta_S = 50.2^\circ$	Chevanceaux, France	HySpex: GSD$_{VNIR}$ = 0.5 m GSD$_{SWIR}$ = 1 m	Mineralogy: kaolinite
	June 2020 $\theta_S = 15.8^\circ$	Cuprite, NV, USA	AVIRIS-NG GSD = 2.9 m	Mineralogy: alunite, kaolinite, iron oxy-hydroxides
	June 2014 $\theta_S = 76.1^\circ$	Mountain Pass, CA, USA	AVIRIS-NG GSD = 3.7 m	Mineralogy: bastnaesite (carbonate-fluoride mineral, REE)
Vegetation	Sept. 2015 $\theta_S = 47.3^\circ$	Fabas Forest, France	HySpex: GSD$_{VNIR}$ = 4 m GSD$_{SWIR}$ = 4 m	Tree species classification (temperate forest, LAI = 3 m²/m²): 20 species
	June 2014 $\theta_S = 17.9^\circ$	Tonzi Ranch, CA, USA (Figure 11)	AVIRIS-NG GSD = 4 m	Mediterranean woodland savannah, (LAI = 0.8 m²/m²): Cab, Car, LMA and EWT
Coastal waters	July 2016 $\theta_S = 31.3 - 32.3^\circ$	Roscoff, France	HySpex GSD$_{VNIR}$ = 0.5 m	Bathymetry
	Sept. 2017 $\theta_S = 42.4^\circ$	Porquerolles Island, France (Figure 13)	HySpex GSD$_{VNIR}$ = 1 m	Bathymetry, Water column estimation: phytoplancton, SPM, CDOM Bottom classification of shallow water.
	July 2019 $\theta_S = 22.5^\circ$	Camargue, France	HySpex GSD$_{VNIR}$ = 1 m	
	June, 2019 $\theta_S = 25.5^\circ$	Champeaux, France	HySpex GSD$_{VNIR}$ = 0.5 m	Classification of intertidal coastal habitats (10 classes)
Urban area	June 2015 $\theta_S = 20.5^\circ$	Toulon, France	NEO-ODIN GSD = 0.5 m	Urban land cover (10 classes)
Industrial site	Sept. 2015 $\theta_S = 58.2 - 60.7^\circ$	Fos-sur-Mer, France	HySpex GSD = 1.4 m	Aerosol plume

	Oct. 2019 $\theta_S = 15.0°$	New Mexico, USA	AVIRIS-C GSD = 6.6 m	Methane leaks

The Fabas forest is composed of six distinct dominant species, including *Quercus* sp., Douglas pine (*Pseudotsuga menziesii*), Laricio pine (*Pinus nigra*), maritime pine (*Pinus pinaster*), Weymouth pine (*Pinus strobus*) and black locust (*Robinia pseudoacacia*). These six species are included in the classification process, along with two additional classes: other conifer and deciduous trees.

For urban areas, ten classes were considered: tile, vegetation, shadow, high reflectance, asphalt, bare soil, pavement, road, stadium and stone.

For shallow water bottom classification, three classes were considered for the Porquerolles site (sand, *Posidonia oceanica* and *Caulerpa taxifolia*), and four classes for Camargue site (sediments, zosters, green algae and red algae).

3. Method

The processing chain is detailed in Figure 2.

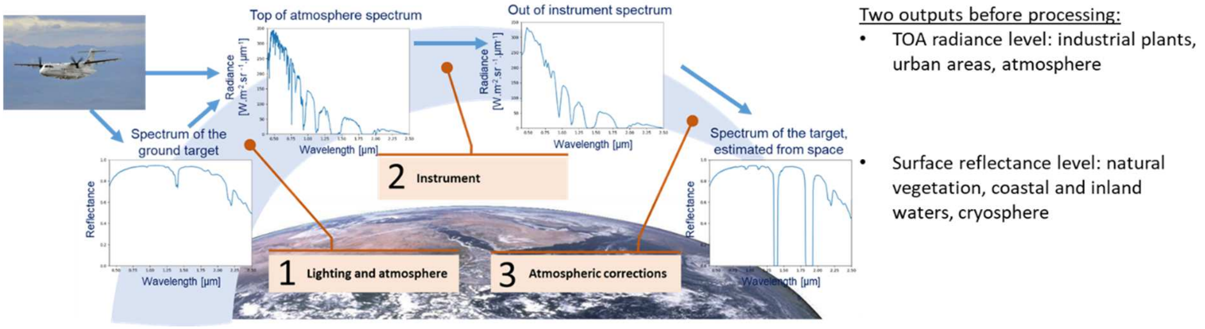

Figure 2. Overview of the end-to-end simulator.

Each application targets one or several variables of interest. For each, a reference value is defined and hyperspectral data (spectra or images) are produced. The end-to-end simulator propagates this data at the top of the atmosphere, just as it would have been acquired by a satellite. Various satellite performances can be simulated. Next, a specific method is applied to retrieve the variable of interest from the satellite data. Finally, the estimated value is compared with the reference value. The discrepancy between the estimation and the reference indicates if the satellite performances meet the application requirements or not. The end-to-end simulator and the processing of each application are detailed below. Figure 3 gives the processing orders and the main parameters used in our simulations.

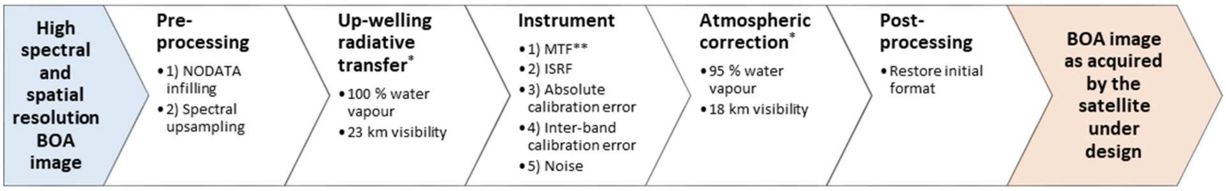

Figure 3. Processing order of the end-to-end simulation chain. *: Not applied on applications based on TOA images (gas content estimation, pan-sharpening), **: Not applied on spectral libraries. ISRF: instrumental spectral response function, MTF: Modulation transfer function

The End-to-End simulator and the processing for each application are detailed in the following.

3.1. End-to-end simulator

The aim of the end-to-end simulator (Figure 2) is to simulate the output signal, in spectral radiance unit, that a sensor can acquire, taking into account its own errors, and then to carry out the atmospheric correction to retrieve the spectral reflectance of the surface.

All data processing was carried out using an end-to-end simulator developed and operated by the French Space Agency (CNES), so that results could be compared (Figure 2). This simulator allows two types of input to be taken into account, depending on the data available for each application: surface reflectance spectra or airborne images expressed in radiance units.

3.1.1. Input top-of-atmosphere spectral radiance

The COMANCHE code (Poutier et al., 2002), based on MODTRAN 5.3 (Berk et al., 2005), was used to calculate the top-of-atmosphere (TOA) radiance. We chose the MODTRAN standard parameters which were coherent with the case studies, i.e. a mid-latitude summer atmosphere and a rural aerosol type with a 23 km horizontal visibility. The solar angular conditions were deduced from the input acquisition conditions (Table 4). A nadir viewing angle was applied for all images since they were all acquired at nadir. The resulting TOA spectral radiance is then processed further to simulate the acquired signals in the hyperspectral and panchromatic channels.

3.1.2. Output top-of-atmosphere spectral radiance

Several scenarios were explored to quantify the instrumental effects on the final products:

- Two signal-to-noise ratios: *optimistic* (O) [100-400] @Lref and *realistic* (R) [50-250] @L_{ref} (Figure 4), with L_{ref} the reference radiance. Gaussian noise with a zero mean and a standard deviation σ was added to the input radiance. σ is equal to:

  $$\sigma(\lambda) = \sqrt{a(\lambda) + b(\lambda).L(\lambda)}$$

  with a a constant noise and b a noise associated to the radiance, both depending on the spectral width, L the TOA radiance, and λ the central wavelength of the spectral band. L_{ref} is defined for an albedo of 0.3, a sun zenith angle of 60° and nadir viewing, a standard mid-latitude winter atmosphere, and a continental aerosol type with a 23 km horizontal visibility.
- Two absolute and interband calibration performances (Figure 5): *threshold* (t) [5% absolute, 2% interband] and *target* (T) [3% absolute, 1% interband].
- Six instrumental spectral response functions (ISRF) defining different sampling strategies, labelled from #1 to #6 (Table 5). Note that the spectral configurations differ only in the SWIR. The ISRF defines how sensible are each spectral channel to every incoming wavelength. The TOA equivalent radiance acquired in a given spectral band i is computed by: $L_i = \frac{\int ISRF_{\mathrm{i}}(\lambda).L(\lambda).d\lambda}{\int ISRF_i\,(\lambda).d\lambda}$ where $L(\lambda)$ is the TOA radiance computed in Paragraph 3.1.1 and

$ISRF_{\mathrm{i}}(\lambda)$ the spectral response of band i. $ISRF_{\mathrm{i}}(\lambda)$ is modeled as a Gaussian function with a central wavelength λ_{c_i} and a full width at half maximum $FWHM_i$. Table 5 provides the spectral step (i.e. the distance between λ_{c_i} and $\lambda_{c_{i+1}}$) and the spectral width ($FWHM$) of each sampling strategy. Note that strategy #5 is a sum of Gaussian functions with a linear increasing $FWHM$. Several ISRFs were tested as the matrix detector might have a limited number of lines to record all the spectral bands. This disadvantage can be overcome by widening the channels spectral width and thus reducing their number. To take into account that the central wavelength of each band may not be known precisely, the calculation includes a constant spectral shift of 1 nm, typical from a spectral calibration error.

Note the instrument parameters used are realistic and that the sensor is technologically feasible. In summary, a scenario is defined by a spectral strategy (#1 to #6), a calibration performance (t for *threshold* or T for *target*) and a SNR (O for *optimistic* or R for *realistic*). Each scenario is then referred to as the triplet (spectral strategy, calibration, SNR). A star indicates that the comment applies to all possibilities in the triplet component. The reference scenario is (#1, T, O), i.e. 10 nm wide spectral channels with the lower calibration errors and the best SNR.

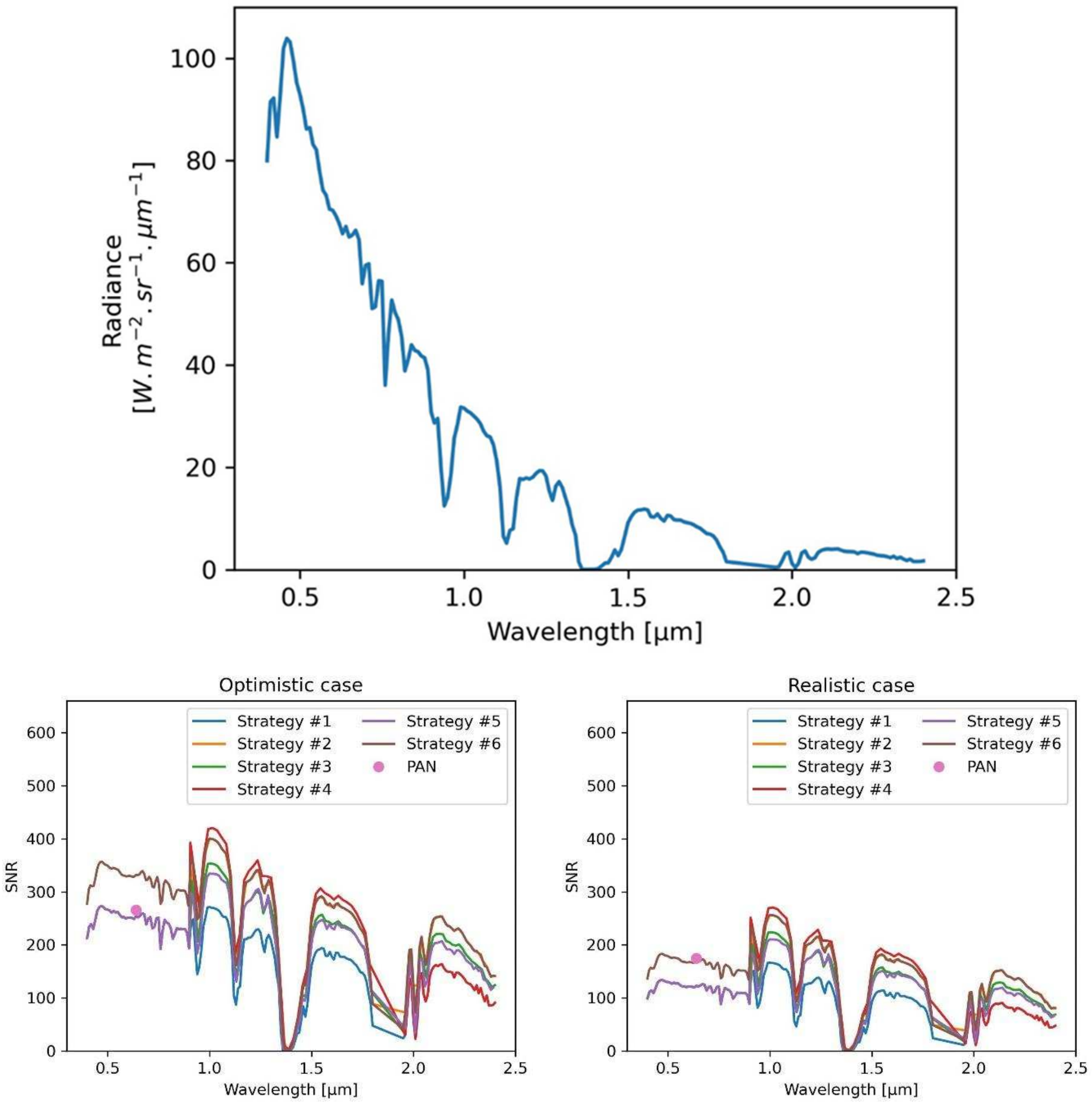

Figure 4. Top: reference spectral radiance, L_{ref}, used to define SNR. Bottom left: optimistic SNR. Bottom right: realistic SNR.

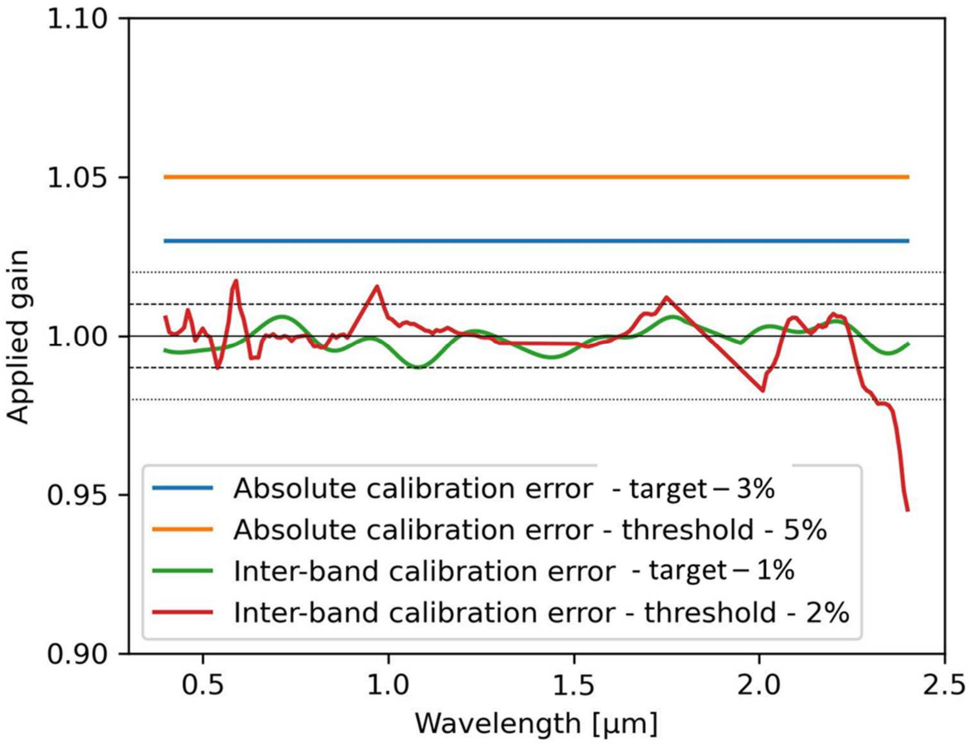

Figure 5. Absolute and interband calibration errors: threshold and target.

Table 5. Spectral sampling strategies. The spectral range from 1850 to 1950 nm is unused.

Sampling Strategy	**VNIR (400 – 900 nm)**			**SWIR (900 – 1850 nm / 1950 – 2400 nm)**		
	Spectral step (nm)	**Spectral width (nm)**	**Number of channels**	**Spectral step (nm)**	**Spectral width (nm)**	**Number of channels**
#1	10	10	51	10	10	136
#2	10	10	51	20	20	68
#3	10	10	51	16	16	85
#4	10	10	51	22 for λ ≤ 1.95 10 for λ > 2.05	22 for λ ≤ 1.95 10 for λ > 2.05	86
#5	10	10	51	12	Linear increase from 14 to 17 nm over [0.9 – 1.3], [1.3 – 1.8], and [1.95 – 2.4],	112
#6	8	16	63	10	20	136

In addition, the instrument introduces some blurring into the image, the magnitude of which depends on the wavelength and is modelled by the modulation transfer function (MTF). Due to the push-broom acquisition mode, the MTF is not equivalent along and across the satellite track (Figure 6). When processing the spectral libraries, the MTF simulation is not activated as only one pixel is processed.

When processing the spectral libraries, MTF simulation is not activated as only one pixel is processed.

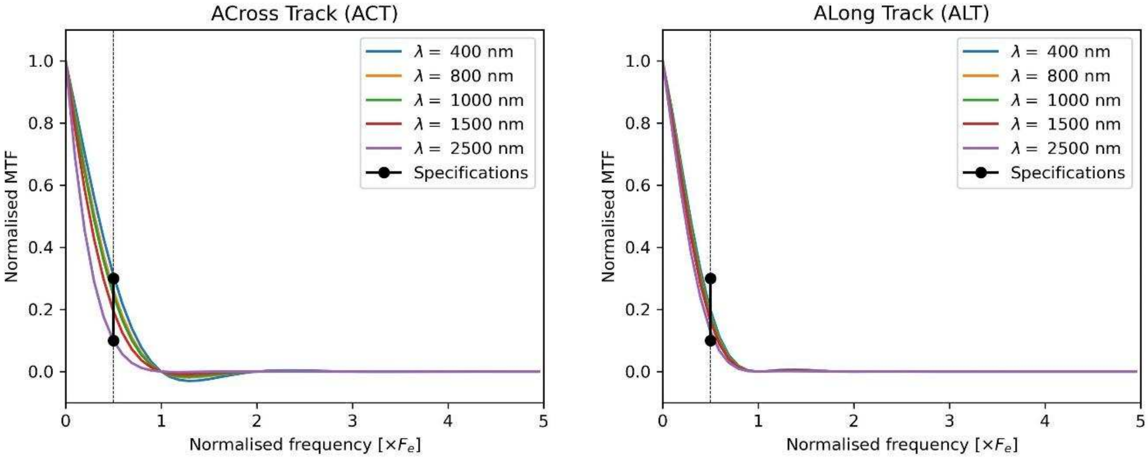

Figure 6. Modulation transfer function (MTF) of five spectral bands of the instrument in the frequency domain.

The instrument also features a panchromatic channel (PAN). Four additional images were generated with two SNR (realistic or optimistic, Figure 4) and two instrumental calibration performances (threshold or target). Figure 7 shows the normalized sensitivity of the panchromatic channel and its point spread function at 639 nm.

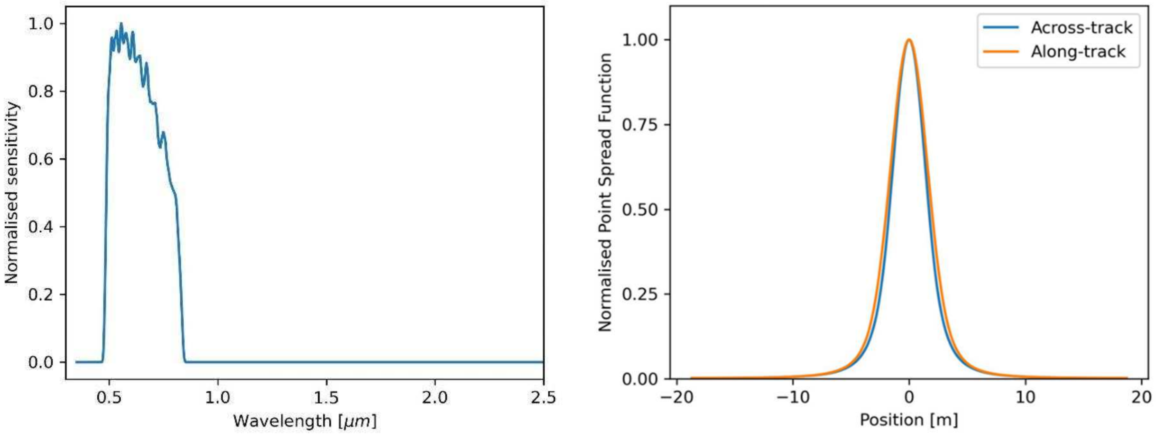

Figure 7. (Left) Normalized sensitivity of the panchromatic channel. (Right) Point spread function at 639 nm.

To summarize the end-to-end processing chain, the input TOA radiance is first affected by the MTF (reduction of the input spatial resolution), then by the ISRF (reduction of the input spectral resolution). At this point, the absolute calibration error as well as the inter-band calibration error are applied. The last step corresponds to the instrumental noise simulation.

In the end, for each input image, this experimental design produced twenty-four simulated images representative of various instrumental performances. However, the sensor design does not yet allow us to take into account other potential defects, such as stray light, geometric errors (geolocation, band registration, etc.), across-track variations in instrument characteristics (MTF, ISRF, etc.) including the smile effect, polarization sensitivity, directional effects induced by slowing down the satellite during acquisition or, and detector defects (remanence, dead pixels, etc.).

3.1.3. Spectral surface reflectance

The complexity of atmospheric correction algorithms allow them to be adapted to different situations. In this study, simulated data or images have been corrected for atmospheric effects with high performance so as not to interfere with the other parameters of interest (i.e., instrument configuration). However, some typical sources of error are accounted for:

- An error of 5 km in horizontal visibility: the upward transfer is performed with a visibility of 23 km and the downward transfer with a visibility of 18 km. Aerosol type remains unchanged.
- A 5% error in the water vapor content: the downward transfer is calculated with 95% of the water vapor content simulated on the upward transfer.

As the upward transfer is done numerically, the atmospheric correction can be carried out with the same performance whatever the target. This choice makes it possible to compare images from one application to another.

3.2. Description of methods by scientific field

For each scientific field covered by this study, Table 6 provides the variables of interest, the input format, the method used to estimate these variables, the bibliographic reference detailing the method and the evaluation criteria.

Table 6. Methods used to retrieve application-related variables. SA: Spectral Analyst, SAM: Spectral Angle Mapper, SD: standard deviation, SFF: Spectral Feature Fitting, SVM: Support Vector Machine, PLS: Partial Least Square, ACE: Adaptive Coherence Estimator, RMSE: Root-Mean-Square Error, PM: Particle Matter.

Scientific domain	Variable of interest	Type of IS inputs (unit)	Method and author	Reference value of the variable of interest	Evaluation criteria
Geosciences	Mineral composition	Image (surface reflectance)	Visual assessment SAM (Kruse et al., 1993) SFF (Clark et al., 1990)	Mineralogical maps of the site	Position and shape of absorption features Identification if SA > 0.7 and SAM < 0.2 Identification if SA > 0.7 and max(RMSE of SFF) > 0.1
	Soil moisture content	Spectra (surface reflectance)	MARMIT model (Bablet et al., 2018)	Laboratory measurements	RMSE between laboratory input and satellite outputs
Vegetation	Tree species classification	Image (surface reflectance)	Supervised classification: SVM with Radial Basis function (Gimenez et al., 2022)	In situ measurements	Mean, RMSE values of Overall Accuracy, F-score over the 24 scenarios and 30 iterations each
	Leaf functional traits	Image (surface reflectance)	Hybrid method using DART/PROSPECT simulations and PLSR (Miraglio et al., 2022)	Traits maps from a high spatial resolution image	RMSE by comparing ISRF #1 and the others ISRF
Coastal zones	Bathymetry	Image (surface reflectance)	HYPIP processing chain (Lennon et al., 2013)	Lidar measurements	SD and RMSE / bathymetric Lidar
	Bathymetry and bio-optical aquatic parameters	Image (surface reflectance)	Hybrid method based on the Lee model (Lee et al., 1999, Minghelli et al., 2020)	Lidar measurements, in situ water characterization	RMSE / in situ data $RE(\%) = \frac{100}{N}\sum_{i=1}^{N}\frac{\lvert\widehat{y_i}-y_i\rvert}{y_i}$ / in situ data
	Classification of intertidal coastal area	Image (surface reflectance)	With and without IS Pansharpening + Fully Constrained Least Square – the endmembers are known (Heinz and Chang, 2001)	Manual in situ classification map	Normalized RMSE on abundance
	Intertidal coastal area	Spectra (surface reflectance)	PLS and discriminant analysis (Lee et al., 2018)	In situ field spectra	Kappa coefficient Overall Accuracy
Urban area	Urban Land Cover 1	Image (TOA radiance)	IS Pansharpening, Random Forest classification (Loncan et al., 2015)	Manual classification	Good classification rate / reference image
	Urban Land Cover 2	Image in TOA radiance unit	Upsampling of the IS image, SVM classification, fusion with PAN (Ouerghemmi et al., 2017)	Manual classification	Mean F-Score over the classes
Industrial site	PM1 Flux of industrial aerosol plume	Image (TOA radiance)	Multitemporal algorithm (Foucher et al., 2019)	In situ measurements	Estimated error High objective: < 80 µg/m^3 Low objective: < 150 µg/m^3
	Methane concentration of industrial plume	Image (TOA radiance)	Plume detection with ACE detector, quantification of the concentration (Nesme et al., 2021)	JPL estimation	Estimated error High objective: < 1000 ppm.m Low objective: < 1500 ppm.m

Cryosphere	Specific Surface Area, equivalent black carbon content of snow	Spectra (surface reflectance)	Hybrid method with TARTES (Dumont et al., 2017)	Simulations	Bias, standard deviation of the estimates / reference inputs
Atmosphere	Water vapor and CO_2	Spectra (TOA radiance)	Optimal estimation theory (Herbin et al., 2013)	Simulations	RMSE
	Aerosols	Spectra (TOA radiance)	GRASP and optimized fitting following the multi-term Least Square Method (Dubovik et al., 2021)	Simulations	RMSE

3.2.1. Geosciences

A first assessment of the impact of instrument characteristics was carried out qualitatively on spectra of representative minerals extracted from the spectral library and image pixels. The positions and shapes of their absorption features enabled us to visually evaluate the different scenarios, in particular with regards to the spectral strategy. Next, a quantitative assessment was carried out using the Spectral Analyst (SA) algorithm in the ENVI software (https://www.nv5geospatialsoftware.com/). This compares the spectra of representative minerals with those of a reference spectral library at the same spectral resolution, resampled according to the spectral characteristics (band positions and full width at half maximum) of the different strategies. This procedure enabled us to assess the impact of instrument calibration and SNR. To compare the spectra, we used two well-known spectral matching techniques called Spectral Angle Mapper (SAM) (Kruse et al., 1993) and Spectral Feature Fitting (SFF) (Clark et al., 1990). SAM determines the spectral similarity between two spectra by treating them as two vectors in a space whose dimensionality is equal to the number of bands, and calculating the angle between these vectors. This technique is insensitive to illumination and albedo effects when used on calibrated reflectance spectra. SFF is based on the least squares method. The reference spectra are scaled to match the unknown spectra after the continuum is removed from both (Clark et al., 1990; Mars and Rowan, 2010). SAM and SFF values are calculated on VNIR (0.4-1.3 µm), SWIR1 (1.3-2.0 µm) and SWIR2 (2.0-2.5 µm) to avoid as far as possible problems associated with atmospheric corrections in the two main water vapor absorption bands around 1.4 and 1.9 µm. This also allows us to focus on spectral ranges where the selected minerals exhibit diagnostic absorption features, which is recommended with these spectral matching techniques. The SA result is a ranked or weighted score, with higher scores indicating greater confidence.

Soil moisture content is estimated by inversion of the MARMIT model, which represents a wet soil as a dry soil covered by a thin layer of liquid water of thickness L (Bablet et al., 2018). The dry soil can be fully or partially covered with water, with a coverage fraction equal to ϵ. The two input parameters of MARMIT, L and ϵ are estimated by minimizing the cost function:

$$\chi^2(L,\epsilon) = \sqrt{\frac{\sum_{\lambda_1}^{\lambda_2}\left(R_{meas}(\lambda) - R_{mod}(\lambda, L, \epsilon)\right)^2}{n_\lambda}}$$

with n_λ the number of wavelengths (or channels), R_{meas} the measured soil reflectance, and R_{mod} the soil reflectance estimated by MARMIT. The lower and upper bounds of the model parameters are 0 and 1 for ϵ, 0 and 0.2 cm for L. A calibration step is required to establish a statistical relationship between the mean water thickness (mean light path) defined as $\varphi = L \times \epsilon$ and the measured SMC. The evaluation of the method consists in retrieving SMC by applying the relation found in the calibration step and comparing it with the measured values. The RMSE is calculated on 160 SMC values ranging from 5 to 85%.

3.2.2. Vegetation

A supervised support vector machine (SVM) classification is applied together with a radial basis function (RBF) kernel to classify tree species on the basis of spectral signatures extracted from the HySpex image and corresponding to the field inventory. Two subsets are randomly generated, a training one (70%) and a validation one (30%). The training subset is used to optimize the RBF-SVM hyper-parameters, C and Gamma. The strategy followed is based on an exhaustive grid search strategy with 5-fold cross validation aimed at maximizing the overall accuracy (OA) of the classifier. The space defined by C values ranging from 10^{-2} to 10^{9} and Gamma values ranging from 10^{-7} to 10 is explored. The model is then trained using the parameters obtained and the training subset. Next, the trained SVM classifier is applied to the validation subset. The method’s performance is evaluated using the OA and F-score, the user and producer accuracy for each class. As the scores can depend on initial conditions, the whole procedure is repeated 30 times and the mean and RMSE of each accuracy score is calculated. Thirdly, the tree species map is produced using the same scheme with the spectral signature dataset for the training and the image for application. Ultimately, the relevance of each of the twenty-four scenarios is evaluated using this classification scheme, and compared using the mean and standard deviation of the accuracy scores obtained.

Leaf functional traits are estimated using a hybrid method based on training a PLSR on the previously described spectral database generated by DART. An automatic determination of the optimal number of latent variables and a selection of the most important variables in the projection design are performed for the PLSR parameterization. To optimize trait extraction, the spectral range is adapted to the influence of each trait: 0.5-0.8 µm for chlorophyll (Cab) and carotenoids (Car), and 1.5–2.4 µm for leaf mass per area (LMA) and equivalent water thickness (EWT) (Miraglio et al., 2022). Then, the optimal trained PLSR is applied on the airborne image to derive inversion maps of leaf traits, and the RMSE is calculated by comparing the reference scenario (#1) with the others (#2 to #6).

3.2.3. Coastal zones

Shallow water bathymetry is estimated in the 400-900 nm range using the SWIM® software developed by Hytech-imaging (Lennon et al., 2013). SWIM® includes modules for the correction of the sun glint at the surface and for the correction of the air/water interface. Both SWIM and HYPIP include modules for uncertainty propagation from the sensor to the final products. Another method is applied to simultaneously estimate bathymetry and bio-optical parameters and perform shallow water bottom classification (Lee et al., 1999; Minghelli et al., 2020). The aquatic bio-optical parameters are chlorophyll, suspended particulate matter (SPM), colored dissolved organic matter (CDOM), depth, bottom sediment abundance, zosters, green and red algae.

A fully constrained least squares (FCLS) unmixing method is also applied to the airborne VNIR image to estimate the abundance of the several seabed species. PLS-DA analysis (Lee et al., 2018) is then used for VNIR-SWIR field spectra to evaluate the discrimination performance of BIODIVERSITY configurations. This method can be applied to datasets with few observations and many explanatory variables (spectral reflectance), as is the case with the spectral library used in this study.

3.2.4. Urban area

Considering that a GSD of 10 m is not sufficient to classify an urban area, a hyperspectral pansharpening method called Gain is first applied (ULC1). It is inspired by the Brovey transform applied to the RGB+PAN case (Saroglu et al., 2004), but has been generalized to the HS+PAN case (Loncan et al., 2015). A supervised classification method (random forest) is then applied to the resulting image. Ten classes are selected, each composed of twenty spectra. The calibration and validation phases follow the k-fold method: random selection of five groups with a uniform distribution of each class, then four groups are used for calibration and the last one for validation. A second urban land cover (ULC2) method is applied. First, a hyperspectral image is oversampled (bilinear interpolation) to a GSD of 2.5 m corresponding to the panchromatic band. Then, a supervised SVM classification is performed. Ten classes are considered. Fifty training samples were selected for each class, to provide a model unbiased by the unbalanced distribution of classes. This number is considered sufficient to obtain efficient classification models, while keeping a sufficient number of validation samples. For each classification, ten iterations of the classification process (involving random selection of training samples) are performed. Then, a fusion process is then applied. The classification results are evaluated by averaging the F-scores over the classes.

3.2.5. Industrial site

Characterization of PM1 aerosols in an industrial plume uses a multi-temporal algorithm (Foucher et al., 2019). The objective is to determine the difference between two images corrected for illumination and viewing angles, acquired in two wind directions to enhance the PM1 plume signature. The differential model depends on aerosol properties, such as radius, single scattering albedo, and concentration. A correlation map (adaptive coherence estimator, ACE) between the temporal differential and the a priori plume signature from different aerosols types is then calculated. The model assumes a constant layer height of 100 m: for a GSD of 10 m, a mass of 1 g would correspond to a concentration of 100 µg/m^3, or a column concentration of 10^{-2} g/m^2. Pixel concentration is estimated using a linear formalism. To validate the estimate, the error must be below a given threshold (Table 5).

Industrial methane plumes are characterized in two stages (Nesme et al., 2021). To validate the estimate, the error must be below a given threshold (Table 5): a low threshold associated with a flow rate of around 30 g/s, a high threshold associated with a flow rate of around 50 g/s. The detection map is built from thresholds on the ACE detector, on the residuals, and on a priori sensitivity. The amount of excess methane is associated with the transmission τ_{gaz} deduced by inversion of the equation:

$$L_g^* = L_{ng}^* \tau_{gaz} \tag{2}$$

with L_g^* the sensor radiance corresponding to excess gas in the optical path and L_{ng}^* the sensor radiance of the same pixel without excess gas, both corrected for atmospheric path radiance.

3.2.6. Cryosphere

The snow surface is characterized by two properties accessible from imaging spectroscopy (Dumont et al., 2017): the specific surface area (SSA), the ratio between the surface area of air-ice and the snow mass and the equivalent black carbon concentration (eBC). The extraction method finds optimal values for the two variables that minimize the difference between a large set of measured reflectance data and TARTES simulations.

3.2.7. Atmosphere

The method for quantifying water vapor and carbon dioxide used the Shannon information content with the formalism proposed by Rodgers (2000). It introduces the theory of optimal estimation, widely described by Herbin et al. (2013). The a priori errors of the CO_2 and H_2O profiles are set at 5% and 10% respectively. The covariance matrix of measurement errors is deduced from instrument performance and accuracy. The latter is related to the radiometric noise expressed by the SNR defined as *Optimistic-Target*, and *Realistic-Threshold*. The accuracy of non-retrieved parameters is set to $\delta T = 1K$, compatible with the typical values used by the European Centre for Medium-Range Weather Forecasts on each layer of the temperature profile for assimilation, and to an uncertainty of 0.5° on the optical path.

The atmospheric aerosol retrieval method uses the GRASP algorithm. The inversion procedure is based on a statistically optimized least squares method and combines the advantages of a variety of approaches (Dubovik, 2004). This method has already been applied to PRISMA images (Litvinov et al., 2021).

4. Results

4.1. Geosciences

Table 7 presents only a representative subset of the results focusing on cases with spectral strategies (#1, #2, #5 and #6) and with *realistic* SNR conditions representing medium and extreme scenarios.

All diagnostic gypsum absorption bands (Table 1) are observed visually. As expected, there is also an impact of smoothing due to a lower spectral resolution on the shape of the secondary 2.21 µm absorption for # 2 and # 6. In terms of quantitative evaluation (Table 7), the SAM score (respectively SFF) is above 0.75 (resp. 0.61) in SWIR1 except for (#2, T, R), and 0.90 (resp. 0.73) in SWIR2. Whatever the scenario, good scores are obtained with SWIR1 except for (#2, T, R) where gypsum is not identified despite a higher SNR (150:1).

Diagnostic absorption of calcite at ~ 2.34 µm is visible for all scenarios but smoothing (#2, #5, and #6) has an impact on shape and position, leading to possible confusion with dolomite, another carbonate, whose absorption is located at ~ 2.33 µm. For all scenarios, secondary absorption at ~ 2.16 µm is very low. Whatever the scenario (Table 7), the SAM score is > 0.88 and the SFF score > 0.73.

The kaolinite doublet (Table 2) is visible for #1 and slightly visible for #5 and #6 for which the weaker absorption at ~ 2.16 µm is attenuated (Figure 8). Confusion with other clay minerals is possible and the crystallinity of kaolinite cannot be characterized because the relative strength of the doublet absorptions is modified. Unfortunately, the kaolinite doublet is no longer visible with #2. According to Table 7, in all scenarios, SAM remains > 0.88 and SFF > 0.76.

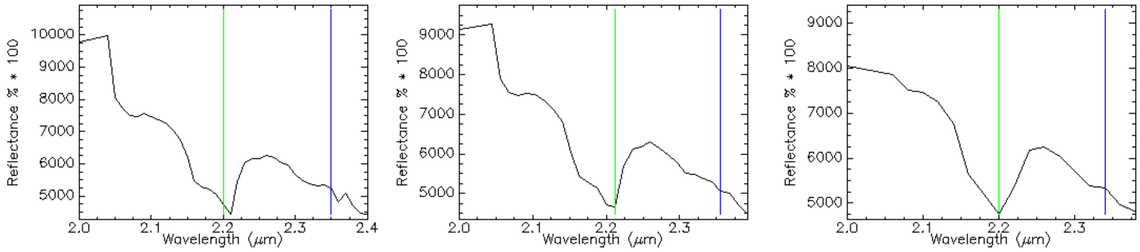

Figure 8. Three kaolinite spectra extracted from the Chevanceaux image, from left to right: (#1,T,R), (#5,T,R), (#2,T,R).

For gypsum, the diagnostic absorption of alunite at 1.76 µm is visible. The other absorptions are visible whatever the scenario, except for (#2, T, R) and (#5, T, R) for which there is a small difference in the right-hand side of the absorption at ~2.16 µm that could hamper identification when using a feature fitting approach. However, high scores are obtained (SAM > 0.85 and SFF > 0.77).

Diagnostic absorptions in the VNIR for goethite and hematite can be identified visually whatever the scenario; meanwhile residual peaks related to atmospheric correction can be corrected. This is confirmed by the fact that SAM can detect goethite (score > 0.73) but hematite detection remains more challenging (score > 0.64). In contrast, SFF cannot detect the corresponding absorption bands (score < 0.53).

All jarosite absorption bands can be detected visually in the infrared, regardless of the scenario tested, leading to SAM scores > 0.79 in the VNIR and > 0.91 in the SWIR. High scores > 0.71 are also achieved with SFF except for (#6,T,R). However, whatever the scenario, the jarosite absorption at ~ 0.45 µm is not clearly visible because it is partially cut off, being located at the edge of the VNIR; this could be a problem for jarosite identification.

The montmorillonite absorption band is clearly visible for all scenarios except for (#2,T,R), where a shape change is detected. SAM and SFF scores are high, > 0.9 and > 0.73, respectively.

Finally, rare-earth elements (bastnaesite, monazite and xenotime) spectra show clear diagnostic absorptions in the VNIR for all scenarios (Figure 9). However, instrument calibration and atmospheric correction errors induce “peaks” located in the absorption bands of dioxygen (~ 0.76 µm) and water vapor (~ 0.94 and ~ 1.13 µm). This explains the poor SFF scores. On the contrary, SAM scores are > 0.67, the lowest score being obtained for (#6,T,R).

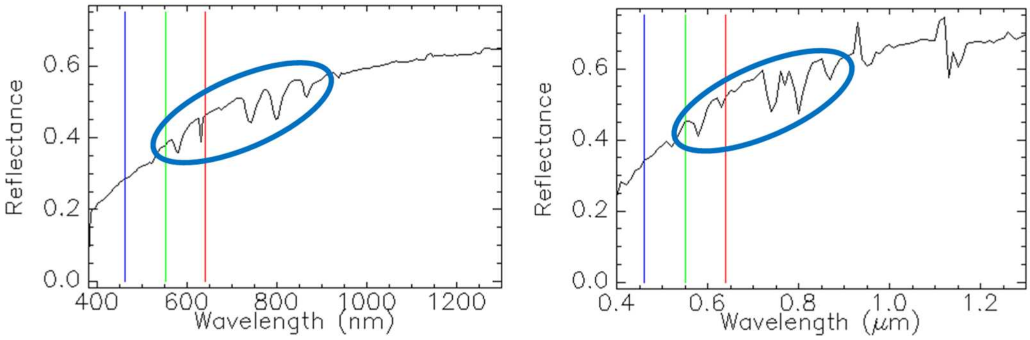

Figure 9. Representative rare-earth elements spectra extracted from the Mountain Pass image. Left: Reference USGS reflectance spectrum. Right: Reflectance for scenario (#1,t,R) after atmospheric correction.

In general, SAM gives better results than SFF, with scores close to 0.9 in the SWIR2. This difference can be explained by the fact that SFF compares the shape of spectra that have undergone continuum removal.

Table 7. SAM/SFF scores from Spectral Analyst (SA) tool (scenario #, t for threshold, T for Target, R for Realistic). Note that SA was performed on a subset of the SWIR2 to avoid the problem caused by CO_2 absorption peaks. In the SWIR1, gypsum and alunite scores are estimated by excluding atmospheric water vapor absorption at 1.4 µm.

Mineral	**(#1, T, R)**			**(#1, t, R)**			**(#2, T, R)**		**(#5, T, R)**		**(#6, T,R)**
	VNIR	SWIR 1	SWIR 2	VNIR	SWIR1	SWIR 2	SWIR1	SWIR 2	SWIR 1	SWIR 2	VNIR
Gypsum		0.77/0.64	0.90/0.77		0.75/0.61	0.90/0.84	0.00/0.58	0.94/0.92	0.96/0.94	0.93/0.88	
Calcite			0.91/0.73			0.88/0.82		0.94/0.92		0.94/0.89	
Kaolinite			0.91/0.78			0.88/0.76		0.92/0.85		0.92/0.85	
Alunite		066/0.49	0.89/0.80		0.43/0.00	0.85/0.77	0.00/0.57	0.88/0.84	0.72/0.94	0.90/0.84	
Goethite	0.73/0.47			0.77/0.53							0.84/0.10
Hematite	0.68/0.27			0.65/0.18							0.64/0.00
Jarosite	0.80/0.71		0.91/0.70	0.79/0.70		0.87/0.71		0.95/0.91		0.93/0.87	0.85/0.01
Montmorillonite			0.90/0.73			0.90/0.79		0.95/0.91		0.94/0.88	
Bastnaesite	0.68/0.40			0.67/0.40							0.61/0.03
Monazite	0.75/0.40			0.75/0.43							0.74/0.15
Xenotime	0.69/0.60			0.71/0.70							0.64/0.21

Estimated soil moisture content is unaffected by the scenarios, with a mean RMSE of 2.6% and a standard deviation of 0.1%.

4.2. Vegetation

The overall accuracy (OA) performance is summarized in Table 8 for tree classification.

Table 8. Overall accuracy performance of tree classification.

	Optimistic		*Realistic*	
	Target	*Threshold*	*Target*	*Threshold*
#1	0.82 ± 0.03	0.83 ± 0.03	0.76 ± 0.04	0.76 ± 0.03
#2	0.81 ± 0.02	0.81 ± 0.03	0.74 ± 0.03	0.74 ± 0.04
#3	0.82 ± 0.03	0.81 ± 0.03	0.75 ± 0.03	0.77 ± 0.02
#4	0.82 ± 0.03	0.81 ± 0.03	0.75 ± 0.03	0.75 ± 0.03
#5	0.82 ± 0.03	0.82 ± 0.03	0.78 ± 0.03	0.76 ± 0.03
#6	0.83 ± 0.04	0.84 ± 0.02	0.77 ± 0.03	0.79 ± 0.04

The overall accuracy of *optimistic* simulations (mean OA value 0.82) is better than that of *realistic* simulations (mean OA value 0.76), whatever the sampling strategy. Performance depends only on the SNR (7% loss between *optimistic* and *realistic*), but not on calibration.

For the estimation of leaf functional traits, the *optimistic* and *realistic* scenarios perform similarly regardless of the trait studied, and are not further discriminated in the following. Figure 12 shows the Cab, Car, LMA and EWT maps obtained with scenario (#1, T, O). Comparison of leaf trait estimation performance for sampling strategies #2 to #6 versus #1 leads to an average RMSE of 2.2 µg/cm² for Cab (average standard deviation of 0.5 µg/cm²), 0.8 µg/cm² for Car (resp. 0.1 µg/cm²), 0.0008 g/cm² for LMA (resp. 0.0003 g/cm²) and 0.0014 g/cm² for EWT (resp. 0.0000 g/cm²). In fact, the same RMSE values are found for EWT whatever the scenario. The performance of *threshold* compared with *target* deteriorates slightly, with an average increase in RMSE of 0.5 µg/cm² for Cab, 0.1 µg/cm² for Car and 0.0004 g/cm² for LMA. Overall, irrespective of calibration performance and SNR level, the quality of leaf trait estimation with scenarios #2 to #6 is similar to that of scenario #1.

These results can be compared to absolute RMSE values of 8.5 µg/cm^2 for Cab under the same conditions (Miraglio et al., 2020), or to an RMSE of 8.1 µg/cm^2 for a sparse coniferous forest (Zarco-Tejada et al., 2019). For Car, Miraglio et al. (2020) found an RMSE of 2.24 µg/cm^2, Zarco-Tejada et al. (2013) an RMSE of 0.9 µg/cm^2 on crops and Asner et al. (2015) an RMSE of 0.2 µg/cm^2 on tropical forests. On tropical forests, Chadwick et Asner (2016) found an RMSE of 0.0020 g/cm^2 and Asner et al. (2015) an RMSE of 0.0023 g/cm^2 for LMA. Buddenbaum et al. (2015) estimated EWT on European beech seedlings with an RMSE of 0.0007 g/cm^2, within a range of 0.001 to 0.008 g/cm^2. Li et al. (2008) retrieved EWT with an RMSE of 0.0132 g/cm^2 from optical libraries and simulated data.

4.3. Coastal zones

For bathymetry, since scenarios #1 to #5 have the same spectral strategy in the VNIR, only scenarios #1 and #6 will be compared. Table 9 summarized the results for the three images used to estimate bathymetry.

Table 9. Bathymetry performance obtained on the three images.

	RMSE (m)					
Site	**Roscoff**		**Porquerolles Island**		**Camargue**	
Scenario	#1-5	#6	#1-5	#6	#1-5	#6
Optimistic, Target	1.0	1.2	1.5	1.2	0.3	0.4
Optimistic, Threshold	1.7	1.8	2.0	1.6	0.4	0.5
Realistic, Target	1.2	1.2	2.2	1.4	0.3	0.4
Realistic, Threshold	1.8	1.8	2.8	1.7	0.4	0.5

Water depth is estimated at between 0 and 10 m in Porquerolles Island and between 0 and 2.5 m in Camargue.

For Roscoff, the (*,T,*) scenarios give better results than the (*,t,*) scenarios (decrease of around 0.7 m). Scenario #6 tends to smooth out the results, with a noise distribution similar to that of scenario #1. The impact of calibration is therefore the most critical factor. The performance of bathymetric products calculated with the *target* calibration is consistently better than that calculated with the *threshold* calibration. Using the best configuration (#1,T,*), bathymetric product performance is close to that calculated with the original HySpex data. The SNR effect is insignificant, but caveats can be made about the impact of noise inherent in the source data, which could have an impact on the calibration present value and noise effects.

For Porquerolles, the *target* calibration gives better results than the *threshold* calibration (Figure 14). The difference between derived bathymetry and the in-situ data is small (RMSE < 2.8 m corresponding to a relative error < 30%). Note, however, that retrieval in *threshold* calibration remains acceptable. Retrieval performance is better for #6 than for #1. For Camargue, the *target* calibration provides 20% better bathymetry retrieval than that obtained with the *threshold* calibrations. The latter is not acceptable: the relative difference between bathymetry retrieval and in-situ data is ~ 80%. Performance is consistently better for sampling strategy #1 than for sampling strategy #6.

For remote sensing of coastal ecosystems, the retrieval of bathymetry using simulated data is always of interest. A relative error < 30% remains satisfactory and is generally accepted by the community (Dekker et al., 2011). A relative error < 20% should ideally be sought to significantly improve understanding of these ecosystems. For the classification of shallow water bottoms, Tables 10 and 11 give the classification results obtained for Porquerolles Island and Camargue.

Table 10. RMSE error for bottom abundance fraction retrieval in Porquerolles Island.

Scenario	Sand (%)	*Posidonia oceanica* (%)	*Caulerpa taxifolia* (%)
(#1,O,T)	29	33	8
(#6,O,T)	28	32	4
(#1,O,t)	30	33	4
(#6,O,t)	29	33	4
(#1,R,T)	38	46	24
(#6,R,T)	29	34	11
(#1,R,t)	30	35	4
(#6,R,t)	28	32	4

Table 11. RMSE error for bottom abundance fraction retrieval in Camargue.

Scenario	SPM (%)	Zoster (%)	Green algae (%)	Red algae (%)
(#1,O,T)	11.	19.	23.	23.
(#6,O,T)	15.	2.	17.	26.
(#1,O,t)	20.	7.	25.	49.
(#6,O,t)	34.	5.	10.	49.
(#1,R,T)	14.	17.	15.	27.
(#6,R,T)	17.	6.	16.	32.
(#1,R,t)	2.	11.	18.	49.
(#6,R,t)	31.	9.	9.	49.

For Porquerolles, the average RMSE found for retrieval of bottom abundance fractions varies according to the background (Figure 14): sand (30-28%), *Posidonia oceanica* (32-46%) and *Caulerpa taxifolia* (4-24%). The lowest RMSE is obtained on the latter with an RMSE < 10% except for (#1,T,R) and (#6,T,R). The best scenarios are (#6,T,O), (#6,T,O), (#1,t,O), (#6,t,O), (#1,t,R) and (#6,t,R). For Camargue, the RMSE error is between 2% and 49% for all scenarios. The retrieval of zoster species (between 2% and 19%) leads to the best results. Overall, the best scenario for estimating the four variables is (#6,T,O). Inversion performance is globally higher for Camargue than for Porquerolles Island. As the bathymetry of Camargue is much lower than that of Porquerolles Island, the TOA radiance is higher, which reduces the influence of sensor noise on retrieval performance. A degradation in sensor calibration induces a significant decrease in inversion performance and thus reduces the ability to correctly derive bathymetry in shallow water. Sensitivity to SNR shows that a strategy involving wider spectral bands is preferred (i.e., Porquerolles Island). The narrow spectral band strategy only has an advantage when SNR is not the limiting factor, typically for shallow water sites such as Camargue. Estimates of abundance fraction of bottom species proved to be inconsistent and non-exploitable (RMSE > 3 m) for bottom depths > 10 m.

For coastal habitat classification, unmixing performance was evaluated on the VNIR hyperspectral image and compared with the reference. RMSE performance is very similar across all scenarios (average RMSE 4.65%, average standard deviation 3.73%). A slight improvement is obtained using pansharpened images (4.26% and 3.40%, respectively). This is not surprising given the high spatial heterogeneity of these areas and the need for fine spatial resolution to improve the accuracy of biological component estimates. The best performances were obtained with (#6,T,O) and (#1,T,O), and the worst with (#1,t,R) with or without prior pansharpening.

Finally, PLS-DA applied to the VNIR-SWIR spectral library on a limited number of scenarios (#1,T,R), (#2,T,R), (#5,T,R), (#1,t,R) led to better performances than those obtained with VNIR images (Kappa ranging from 0.76 to 0.92). Among the four scenarios tested, the best performance is obtained with (#2,T,R), underlining the importance of SNR in the discriminant process.

4.4. Urban land cover

Whatever the scenario, performance is very similar. With the ULC1 method (Figure 15), overall accuracy performance is between 66 and 67% with *target* calibration and ~ 65% ± 0.1 with *threshold* calibration. With the ULC2 method, all scenarios are similar, with an F-score of ~ 54% ± 0.1. This classification is based primarily on the overall spectral shape of the reflectance and is therefore insensitive to spectral strategies.

4.5. Industrial site

To estimate PM1 aerosols, only the VNIR is used. Consequently, only sampling strategies #1 and #6 are considered. First, the detection performance of the aerosol plumes present in the images is evaluated by estimating the percentage of true positives and false positives compared with the airborne image used as a reference (Table 12). As performance does not depend on calibration, only an average value is given.

Table 12. Detection rate compared with the airborne image.

	True positive (%)	**False positive (%)**
#1, *Optimistic*	56	19
#6, *Optimistic*	64	23
#1, *Realistic*	64	21
#6, *Realistic*	67	23

The detection rate varies from 56% to 67% and the false detection rate from 19% to 23%. There is no trend between these values and changes in the instrument specifications, especially with the optimization of segmentation parameters. Table 13 shows the average sensitivity to aerosol properties estimated from the differential image for #1 and #6. This includes uncertainty due to instrumental mode, native noise, registration errors and radiative transfer model assumptions. This image was acquired with a high sun zenith angle and a low spatial extent of the plume. With this particular geometry, the downward solar flux does not pass through the plume, leading to poor soot estimation whatever the strategy.

Table 13. Average sensitivity to PM1 mass concentration for the aerosol model studied.

Scenario	**Concentration ($\mu g/m^3$) Known aerosol type**	**Radius (nm)**	**Absorptance (%)**	**Concentration ($\mu g/m^3$) Unknown aerosol type**
(#1,T,O)	73	42	30	140
(#6,T,O)	74	43	40	160
(#1,t,O)	91	90	5	145
(#6,t,O)	92	57	4	140
(#1,T,R)	82	45	30	280
(#6,T,R)	79	53	40	190
(#1,t,R)	106	100	50	260
(#6,t,R)	98	70	50	170

When the aerosol model is known, the high objective of 80 $\mu g/m^3$ is reached for (*,T,O), and the acceptable low objective of 150 $\mu g/m^3$ is reached for all scenarios. However, when the aerosol model is unknown (uncertainties in radius and soot fraction), the increase in uncertainty depends on the sensitivity of the estimate of aerosol radius and soot content. Only scenarios (#1,T,O), (#1,t,O) and (#6,t,O) meet the low objective.

Table 14 presents the methane estimates.

Table 14. Methane abundances (ppm.m) for each scenario. Note that the reference value obtained from the airborne image is 510 ppm.m.

	Optimistic		*Realistic*	
Sampling	***Target***	***Threshold***	***Target***	***Threshold***
#1	900	980	1330	1490
#2	980	1050	1300	1510
#3	900	1120	1310	1420
#4	930	1020	1330	1410
#5	890	1000	1250	1450
#6	800	860	1070	1160

In the case of a *realistic* SNR and a *threshold* value for calibration, sampling strategy #3 should achieve the low objective of 1500 ppm.m. Sampling strategy #1 is better than #3 in the case of high SNR (*optimistic*), but has no advantage in the case of low SNR (*realistic*). Sampling strategy #6 performs better at all SNRs and should provide results within the high objective of 1000 ppm.m. However, due to the low spectral resolution, it leads to an increase in false alarms compared to the other strategies, which induced a bias in the flow rate estimation. For sampling strategies #1 to #5, the high objective is only achieved in the case of high SNR (*optimistic*).

4.6. Cryosphere

Table 15 shows the retrieval results for specific surface area (SSA) and equivalent black carbon (eBC) concentration.

Table 15. Mean bias and standard deviation on retrieved SSA and eBC. The SSA reference value is 2 ± 1 m²/kg. The black carbon reference value is 18 ± 14 ng/g.

	Optimistic		Realistic	
Variable	(*,T,O)	(*,t,O)	(*,T,R)	(*,t,R)
SSA (m²/kg)	4 ± 2	7 ± 4	4 ± 3	8 ± 4
eBC (ng/g)	84 ± 56	102 ± 64	83 ± 56	101 ± 64

The results show that instrumental noise and sampling strategy have a negligible effect compared to calibration errors. SSA retrieval is generally satisfactory, while eBC concentration retrieval is more challenging. In some cases, degradation of the spectral strategy slightly modifies sensitivity to other errors. Thus, a high-performance calibration should enable these two key parameters to be estimated, whereas a low-performance calibration will only give access to SSA. The retrieval of SSA and eBC concentration is not affected by the change in spectral resolution from 10 to 20 nm in the SWIR.

4.7. Atmosphere

Table 16 summarizes the total uncertainties of the H_20 and CO_2 atmospheric columns. As the variations in performance are not very large, only the two extreme cases (*,T,O) and (*,t,R) are shown.

Table 16. Mean error and standard deviation on H_20 and CO_2 estimates calculated for the six sampling strategies.

	H_20 (%)		**CO_2 (%)**	
Scenario	(*,T,O)	(*,t,R)	(*,T,O)	(*,t,R)
	4.5 ± 0.8	5.7 ± 1.0	2.3 ± 0.2	2.5 ± 0.1

For water vapor, whatever the sampling strategy, the degradation in SNR and image quality leads to a slight increase in the average uncertainty from 4.5 to 5.7%. Total uncertainty on the tropospheric CO_2 profile is minimum at around 2.0 with (#1,T,0), corresponding to an uncertainty of 8 ppm on the estimated tropospheric CO_2 column. It is maximum at around 2.6 with (#2,T,R), corresponding to an uncertainty of 10.5 ppm on the estimated tropospheric CO_2 column. Thus, sampling strategy #1 is the best option, while #2 is the least favorable. In contrast to H_2O, the best SNR is preferable to spectral resolution for a better estimation of the tropospheric CO_2 column. Finally, in the case of simultaneous restitution of both gas concentrations, the choice of spectral strategy will depend mainly on the measurement noise.

Figure 10 shows retrieved versus assumed AOT in the forward radiance simulations, the former thus representing the reference (true) values, at 492 nm and 865 nm. Consistently good spectral retrieval indicates correct aerosol model identification. The figure shows the AOT correlations for SNR =200 (spectral bands centered on 419, 441, 492 and 546 nm) and SNR = 100 (spectral bands centered on 669, 770, 865 and 2190 nm) for the scenario (#1,T,R). A slight degradation compared to the noise-free case (not presented here) was noted in the simulations. At the same time, the retrieved AOT values and spectral dependence are reasonably good: R is ~ 0.99 and RMSE from 0.023 to 0.036. These performances are considered to be of reasonable quality, since the same simulations, but without noise, led to RMSEs of 0.015 and 0.025, demonstrating that intrinsic GRASP uncertainty explains a large part of the RMSE. With an SNR of 50, the retrieval convergence algorithm is very poor for all channels.

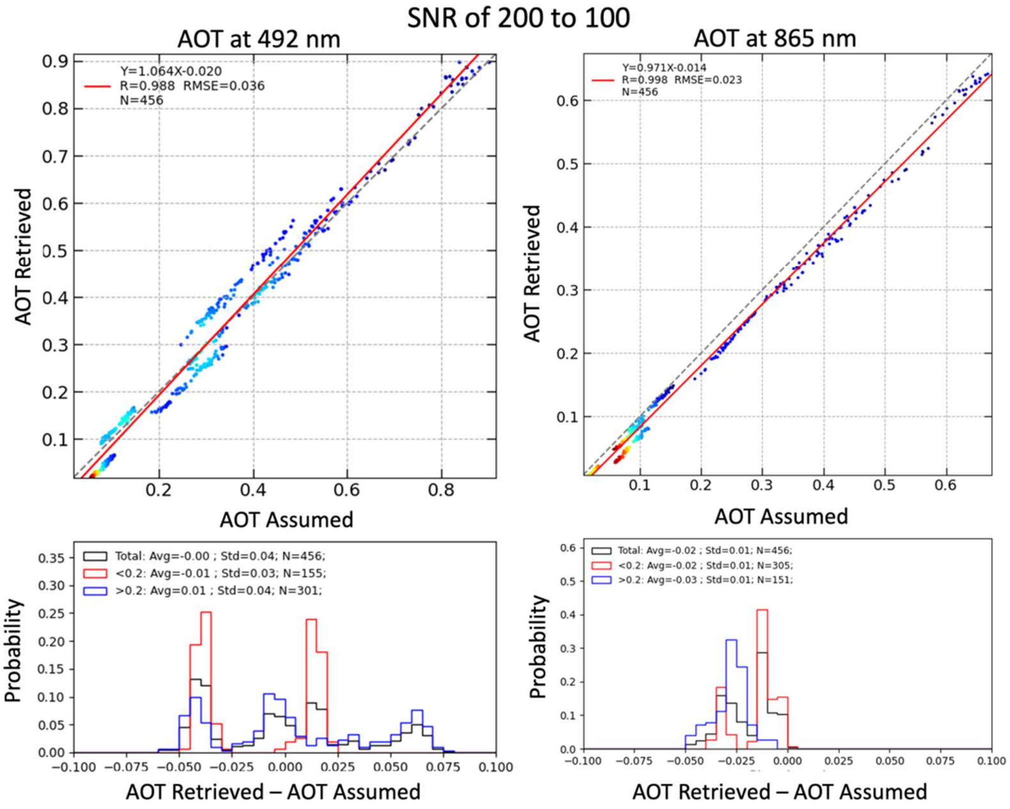

Figure 10. Top: Correlation between retrieved and assumed aerosol optical thickness (AOT) in forward radiance simulations for SNR = 200 (spectral bands centered on 419, 441, 492 and 546 nm) and SNR = 100 (spectral bands centered on 669, 770, 865 and 2190 nm). AOTs are presented at 492 nm and 865 nm. R is the correlation coefficient, RMSE the root mean square error, N the number of points. Bottom: Histograms of absolute differences in AOT (black for all, red for AOT < 0.2 and blue for AOT > 0.2).

5. Discussion

5.1. End-to-end simulation

These end-to-end simulations were performed with realistic instrument characteristics. All products simulated in this exercise used the same end-to-end processing chain, with similar and realistic instrumentation parameters, which facilitated comparisons between the different applications. This work was based on 24 instrument configurations × 27 spectral datasets (22 images + 5 spectral libraries) leading to 648 simulations with different (spectral strategy, calibration performance and SNR) combinations. However, some limitations were identified. One of the first limitations was that all the instrumental defects were not taken into account such as the straylight, the geometrical errors (geolocation, band co-registration, etc.), the across-track variations of the instrument characteristics (MTF, ISRF, etc. including the smile effect for instance), the polarization sensitivity and the detector defects (such as remanence, dead pixels, etc.). Another limitation was the potential overestimation of the performance of the atmospheric correction. Only the water vapor content and the aerosols load errors were considered. The following sources of errors have been neglected: carbon dioxide abundance, aerosol type and the environment effects. Some applications may show better performance here than the ones actually achievable on satellite images. However, the comparison between applications and between different instrumental configurations should remain relevant. Another limitation of this approach was to consider that the performance of the atmospheric correction was constant whatever the performance of the instrument. In practice, the degradation of the instrument will also degrade the atmospheric correction, and will therefore affect the final products even more. The quality of the atmosphere correction was closely related to the calibration performance because the atmospheric water vapor correction uses absorption bands that must be calibrated. But the calibration of bands affected by the atmosphere is more difficult with methods based on ground acquired data (known as vicarious methods), and thus dedicated on-board calibration facilities are required.

5.2. Dependence to the application methods and their input datasets

The results of this study were obtained with specific estimation methods on specific input datasets. The relative performances observed in this context gave valuable information for the satellite design with seven applications covered; but further work will be required to consolidate the conclusions at an even larger scale. For coastal habitat classification, the SWIR spectral range improved classification performance when using spectral libraries. This observation needs to be evaluated at the image level. SMC was estimated with the MARMIT model (Bablet et al., 2018) but an updated version called MARMIT-2 is now available (Dupiau et al., 2021) and could improve our results. Impurities in snow were not well estimated, one reason being related to the choice of the inverse method, so future work would focus on developing a new and more adapted method. The urban area classification was performed using the hyperspectral pansharpening method named GAIN. The presence of mixed pixels limited the performance of the method. Constans et al. (2021) proposed a new method handling mixed pixels which will be evaluated in the future.

5.3. Synthesis of the results

Table 17 summarizes the results. This is followed by discussions on spectral strategy (§5.3.1), SNR (§5.3.2) and calibration performance (§5.3.3).

Table 17. Summary of thematic performance by strategy. The color code is as follow: 🟩 indicates that performance is achieved, 🟧 indicates that performance is around the objective threshold, 🟥 indicates that performance is below the objective threshold. When necessary, the objective threshold (Δ) is indicated in the first row.

	Optimistic		Realistic	
Thematic	**Target**	**Threshold**	**Target**	**Threshold**
Mineralogy 11 minerals	🟩1, 🟥2, 🟥3, 🟩4, 🟧5, 🟧6	🟩1, 🟥2, 🟥3, 🟩4, 🟧5, 🟧6	🟩1, 🟥2, 🟥3, 🟩4, 🟧5, 🟧6	🟩1, 🟥2, 🟥3, 🟩4, 🟧5, 🟧6
Soil Moisture Content $\Delta SMC/SMC=10\%$	🟩1, 🟩2, 🟩3, 🟩4, 🟩5, 🟩6	🟩1, 🟩2, 🟩3, 🟩4, 🟩5, 🟩6	🟩1, 🟩2, 🟩3, 🟩4, 🟩5, 🟩6	🟩1, 🟩2, 🟩3, 🟩4, 🟩5, 🟩6
Tree Species Classification 8 classes	🟩1, 🟩2, 🟩3, 🟩4, 🟩5, 🟩6	🟩1, 🟩2, 🟩3, 🟩4, 🟩5, 🟩6	🟩1, 🟩2, 🟩3, 🟩4, 🟩5, 🟩6	🟩1, 🟩2, 🟩3, 🟩4, 🟩5, 🟩6
Forest EBV				
$\Delta Cab \sim 8\ \mu g.cm^2$	🟩1, 🟩2, 🟩3, 🟩4, 🟩5, 🟩6	🟩1, 🟩2, 🟩3, 🟩4, 🟩5, 🟩6	🟩1, 🟩2, 🟩3, 🟩4, 🟩5, 🟩6	🟩1, 🟩2, 🟩3, 🟩4, 🟩5, 🟩6
$\Delta Car \sim 1\text{-}2\ \mu g.cm^2$	🟧1, 🟧2, 🟧3, 🟧4, 🟧5, 🟧6	🟧1, 🟧2, 🟧3, 🟧4, 🟧5, 🟧6	🟧1, 🟧2, 🟧3, 🟧4, 🟧5, 🟧6	🟧1, 🟧2, 🟧3, 🟧4, 🟧5, 🟧6
$\Delta EWT \sim 0.001\ g.cm^2$	🟧1, 🟧2, 🟧3, 🟧4, 🟧5, 🟧6	🟧1, 🟧2, 🟧3, 🟧4, 🟧5, 🟧6	🟧1, 🟧2, 🟧3, 🟧4, 🟧5, 🟧6	🟧1, 🟧2, 🟧3, 🟧4, 🟧5, 🟧6
$\Delta LMA \sim 0.002\ g.cm^2$	🟩1, 🟩2, 🟩3, 🟩4, 🟩5, 🟩6	🟩1, 🟩2, 🟩3, 🟩4, 🟩5, 🟩6	🟩1, 🟩2, 🟩3, 🟩4, 🟩5, 🟩6	🟩1, 🟩2, 🟩3, 🟩4, 🟩5, 🟩6
Bathymetry $\Delta Depth<1$ m	🟩1, 🟩2, 🟩3, 🟩4, 🟩5, 🟩6	🟥1, 🟥2, 🟥3, 🟥4, 🟥5, 🟥6	🟧1, 🟧2, 🟧3, 🟧4, 🟧5, 🟧6	🟥1, 🟥2, 🟥3, 🟥4, 🟥5, 🟥6
Bottom Classification of Shallow Water 6 classes	🟩1, 🟩2, 🟩3, 🟩4, 🟩5, 🟩6	🟧1, 🟧2, 🟧3, 🟧4, 🟧5, 🟧6	🟧1, 🟧2, 🟧3, 🟧4, 🟧5, 🟧6	🟥1, 🟥2, 🟥3, 🟥4, 🟥5, 🟥6
Classification of Coastal habitats (without Fusion)	🟩1, 🟩2, 🟩3, 🟩4, 🟩5, 🟩6	🟩1, 🟩2, 🟩3, 🟩4, 🟩5, 🟩6	🟩1, 🟩2, 🟩3, 🟩4, 🟩5, 🟩6	🟩1, 🟩2, 🟩3, 🟩4, 🟩5, 🟩6
Urban Land Cover 10 classes	🟩1, 🟩2, 🟩3, 🟩4, 🟩5, 🟩6	🟩1, 🟩2, 🟩3, 🟩4, 🟩5, 🟩6	🟩1, 🟩2, 🟩3, 🟩4, 🟩5, 🟩6	🟩1, 🟩2, 🟩3, 🟩4, 🟩5, 🟩6
Industrial Plant Gas $\Delta CH_4 = 1000$ ppm.m	🟩1, 🟩2, 🟩3, 🟩4, 🟩5, 🟩6	🟩1, 🟩2, 🟩3, 🟩4, 🟩5, 🟩6	🟧1, 🟩2, 🟩3, 🟩4, 🟩5, 🟩6	🟩1, 🟥2, 🟩3, 🟩4, 🟩5, 🟩6
Industrial Plant Gas $\Delta CO_2 = 150000$ ppm.m	🟩1, 🟩2, 🟩3, 🟩4, 🟩5, 🟩6	🟩1, 🟩2, 🟩3, 🟩4, 🟩5, 🟩6	🟧1, 🟩2, 🟩3, 🟩4, 🟩5, 🟩6	🟩1, 🟥2, 🟩3, 🟩4, 🟩5, 🟩6
Industrial Plant Aerosol: aerosol model known				
$\Delta AOT=80 \mu g/cm^2$	🟩1, 🟩2, 🟩3, 🟩4, 🟩5, 🟩6	🟩1, 🟩2, 🟩3, 🟩4, 🟩5, 🟩6	🟥1, 🟥2, 🟥3, 🟥4, 🟥5, 🟥6	🟥1, 🟥2, 🟥3, 🟥4, 🟥5, 🟥6
$\Delta AOT=150 \mu g/cm^2$	🟩1, 🟩2, 🟩3, 🟩4, 🟩5, 🟩6	🟩1, 🟩2, 🟩3, 🟩4, 🟩5, 🟩6	🟩1, 🟩2, 🟩3, 🟩4, 🟩5, 🟩6	🟩1, 🟩2, 🟩3, 🟩4, 🟩5, 🟩6
Industrial Plant Aerosol: aerosol model not known $\Delta AOT=150 \mu g/cm^2$	🟩1, 🟩2, 🟩3, 🟩4, 🟩5, 🟩6	🟩1, 🟩2, 🟩3, 🟩4, 🟩5, 🟩6	🟥1, 🟥2, 🟥3, 🟥4, 🟥5, 🟥6	🟥1, 🟥2, 🟥3, 🟥4, 🟥5, 🟥6
Cryosphere: $\Delta SSA=2\ m^2.kg^{-1}$	🟩1, 🟩2, 🟩3, 🟩4, 🟩5, 🟩6	🟧1, 🟧2, 🟧3, 🟧4, 🟧5, 🟧6	🟩1, 🟩2, 🟩3, 🟩4, 🟩5, 🟩6	🟧1, 🟧2, 🟧3, 🟧4, 🟧5, 🟧6
Cryosphere $\Delta eBC=18\ nb.g^{-1}$	🟧1, 🟧2, 🟧3, 🟧4, 🟧5, 🟧6	🟥1, 🟥2, 🟥3, 🟥4, 🟥5, 🟥6	🟧1, 🟧2, 🟧3, 🟧4, 🟧5, 🟧6	🟥1, 🟥2, 🟥3, 🟥4, 🟥5, 🟥6
Atmospheric Gas H_2O, $\Delta H_2O/H_2O$ (10%)	🟩1, 🟩2, 🟩3, 🟩4, 🟩5, 🟩6	Not tested	Not tested	🟩1, 🟩2, 🟩3, 🟩4, 🟩5, 🟩6
Atmospheric Gas CO_2	🟩1, 🟩2, 🟩3, 🟩4, 🟩5, 🟩6	Not tested	Not tested	🟩1, 🟩2, 🟩3, 🟩4, 🟩5, 🟩6
Atmospheric Aerosol with revisit or auxiliary (type, abundance)	🟩1, 🟩2, 🟩3, 🟩4, 🟩5, 🟩6	🟩1, 🟩2, 🟩3, 🟩4, 🟩5, 🟩6	🟩1, 🟩2, 🟩3, 🟩4, 🟩5, 🟩6	🟩1, 🟩2, 🟩3, 🟩4, 🟩5, 🟩6

5.3.1. Spectral strategy

As Table 5 shows, the different spectral strategies are fairly equivalent over the VNIR and variable over the SWIR. Two types of results can be distinguished, depending on the variable to be extracted.

First, when searching for local spectral features characterizing a material, the method's performance is highly dependent on the spectral strategy. This is the case for mineralogy, where the kaolinite doublet can only be discriminated with sampling strategies #1 and #4. Sampling strategies #5 and #6 are acceptable for some minerals, but lead to confusions for others. Sampling strategies #2 and #3 fail to achieve the objectives set for mineralogy. These results confirm the work of Swayze et al. (2003), who predict a spectral resolution of 10 nm to discriminate clays and more specifically kaolinite. Sun et al. (2006) estimate that a spectral sampling interval of 8.2 nm and an SNR > 200 between 1.95 and 2.4 µm does not affect the identification of the 15 minerals tested. Furthermore, kaolinite (resp. dickite) cannot not be detected if the spectral sampling interval is > 16.4 nm (resp. 12.3 nm). On the other hand, Chabrillat et al. (2002) showed that a spectral resolution of 17 nm reduces the ability to detect kaolinite in a mixture, as the Al-OH doublet is not well sampled, but allows the detection of smectites or illites. Although the spectral resolution of HyMAP (~17 nm) is almost half that of AVIRIS (~10 nm), Kruse (2002) showed that both sensors can separate calcite from dolomite and the three varieties of sericite present in Northern Grapevine mountains (NV, USA).

Spectral sampling #2 is not recommended for H_2O and CO_2 estimates, but the best spectral strategy depends strongly on SNR. Spectral sampling #6 is not recommended for bathymetry and aerosol plume. For the gas plume, spectral sampling #5 fails to detect CH_4 accurately (< 1500 ppm.m).

Methods based on the use of the global spectral shape do not depend on the spectral sampling strategy. This is the case for SMC, tree species classification, tree functional trait estimation, bathymetry, shallow water bottom classification, coastal habitat classification, urban land cover, snow and ice characterization, and aerosols. They depend on either the SNR (bathymetry, classification in general) and/or instrument calibration (bathymetry, classification, characterization of industrial plant and snow). Gomez et al. (2018) evaluated the predictive performance of clay soil properties as a function of spectral configuration and showed that it did not depend on spectral sampling, which ranged from 5 to 100 nm. For species identification, Jianxin Jia et al. (2022) compared the classification performance of eleven species with different bandwidths, which ranged from 9.6 to 153.6 nm. They conclude that classification performance is similar for a bandwidth ranging from 9.6 to 19.2 nm, and if the bandwidth is widened, leading to a similar SNR, spatial resolution can be improved. Serbin et Townsend

(2020) recommended spectral sampling and FWHM of 10 nm for leaf pigments (Cab, Car), of 20 nm for EWT and LMA. These results are in line with our results.

5.3.2. Signal-to-noise ratio

For applications using specific absorption bands, performance depends firstly on SNR (*optimistic*/*realistic*) and secondly on calibration performance. Estimates are slightly degraded between *optimistic* and *realistic*, but most of the applications tested depend little or not on the SNR studied, with the exception of bathymetry and shallow water classification due to low reflectance, carbon dioxide and methane.

For mineralogy, according to Kruse et al. (2002), an SNR of at least 100 in the SWIR is required for mineral detection, so the *realistic* SNR is slightly above this limit, while the *optimistic* SNR is higher, as for the PRISMA or EnMap instruments (Peyghambari and Zhang, 2021). Below this value, applications such as calcite-dolomite or clay discrimination, mineral mapping, soil component discrimination or sediment detection is critical (Transon et al., 2018). Thus, such discrimination will be difficult if not impossible with the current SNR of the mission. Sun et al. (2006) estimate that an SNR of at least 200 at 2100 nm is required to map minerals with linear spectral unmixing. Chabrillat et al. (2002) show that detection of dark clays or dark Granero shales requires an SNR > 600 to detect them partially.

5.3.3. Calibration performance

Most of the applications tested depend little or not at all on the calibration scenarios, with the exception of bathymetry (not filled for *threshold*) and cryosphere (equivalent black carbon concentration not estimated with *threshold*). A slight loss in performance was observed between *target* and *threshold* calibrations. Whatever the spectral strategy, scenarios with *target* calibration performance and *optimistic* SNR clearly delivered similar performance. Scenarios with *threshold* calibration performance and *optimistic* SNR and scenarios with *target* calibration performance and *realistic* SNR represent a good compromise. With the SNR used in this study, the impact of instrument calibration on mineralogy is low. There is no obvious difference between *target* and *threshold* cases. Spectral calibration and atmospheric correction errors should be taken with care, as they can induce peaks at H_2O and CO_2 wavelengths, which can be problematic for the identification of certain minerals, depending on the algorithm selected.

6. Conclusion

CNES is working on a hyperspectral mission (0.40-2.45 µm, 10 m GSD, 10 km swath) with a panchromatic camera (2.5 m GSD). A phase A study has just been completed in mid-2022. A large French scientific community has been involved to optimize the instrument design. Taking into account the technological constraints of the SWIR detector, an analysis of several spectral sampling strategies was conducted to assess their impact on end-user applications (mineralogy, vegetation, coastal area, urban area, industrial site, cryosphere and atmosphere).

An end-to-end simulator has been developed to generate the hyperspectral images that the satellite under design will acquire, taking into account the main instrumental effects. It will be improved by including other sources of error when the instrument design matures.

It has also been shown that most of applications can be realized with an optimistic SNR level and target calibration, whatever the sampling scenario. With *optimistic* SNR and *threshold* calibration, most applications have been achieved, with the exception of bathymetry and cryosphere (eBC). With *realistic* SNR and a *target* calibration, most applications have been achieved, with the exception of industrial aerosols. Finally, with *realistic* SNR and *threshold* calibration, most applications have been achieved, with the exception of bathymetry, bottom classification of shallow water, industrial aerosol and cryosphere (eBC). We also found that some spectral strategies were unable to track certain spectral features for mineralogy and industrial gas estimation. All scenarios tested were simulated with the same atmospheric uncertainty on water vapor content and aerosol optical thickness, regardless of instrument configuration.

Based on these results, CNES is studying the best compromise for designing the hyperspectral sensor that will meet the objectives of the priority applications. These preliminary conclusions need to be confirmed by further studies, in particular taking into account the dependence between scenario and atmospheric correction performance, as well as improvements in estimation methods. Other applications will be evaluated, such as crop characterization, pollution monitoring and plastic detection.

Appendix

This appendix completes the results obtained in this work: maps of leaf functional traits, shallow water bottom classification and urban land cover.

Figure 11 is an RGB image of the Tonzi site. Figure 12 shows the Cab, Car, LMA and EWT maps estimated on QUDO with sampling strategy (#1,T,O).

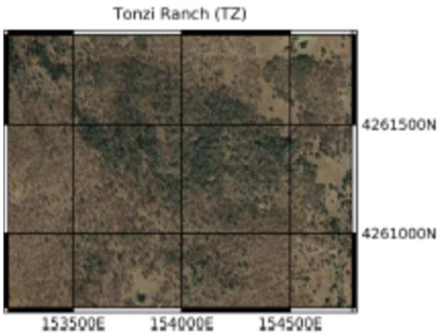

Figure 11. Tonzi site (CA, USA)

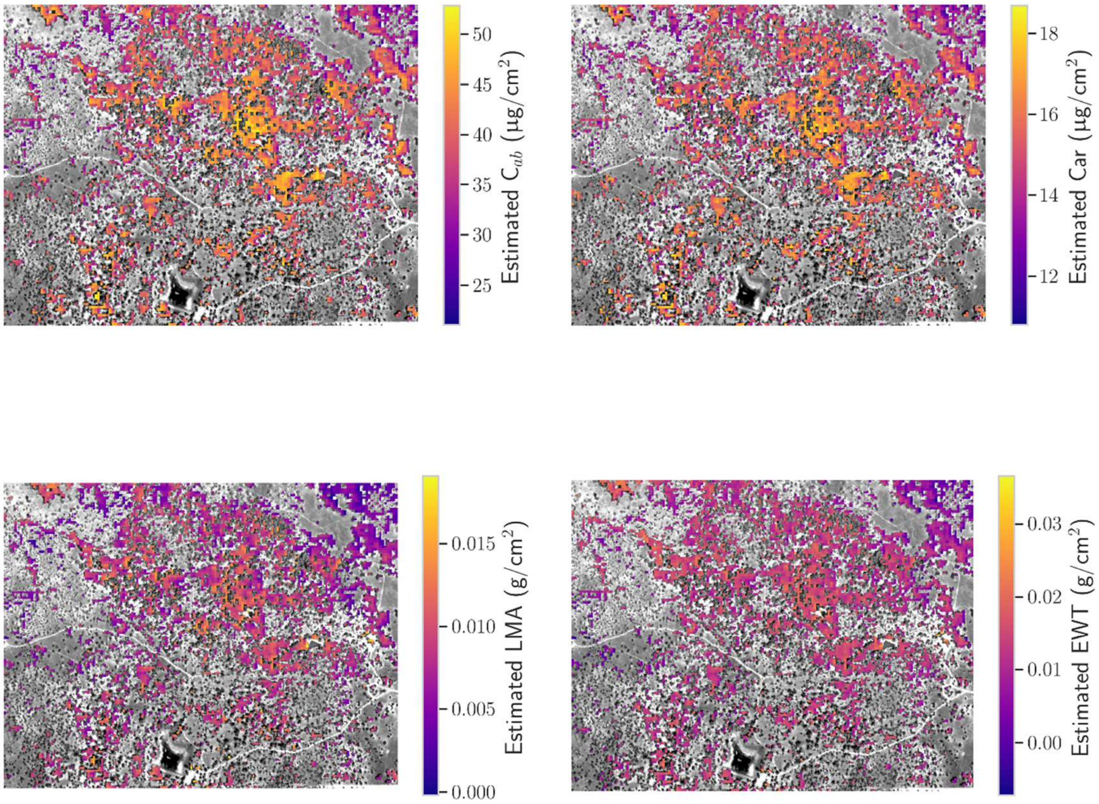

Figure 12. Leaf functional trait maps obtained with scenario (#1,T,O). Top left: Cab. Top right: Car. Bottom left: LMA. Bottom right: EWT.

Figure 13 is an RGB image of the Porquerolles site. Figure 14 shows maps of water parameters (chl, SPM, CDOM), depth and seabed abundance with (#1,T,O).

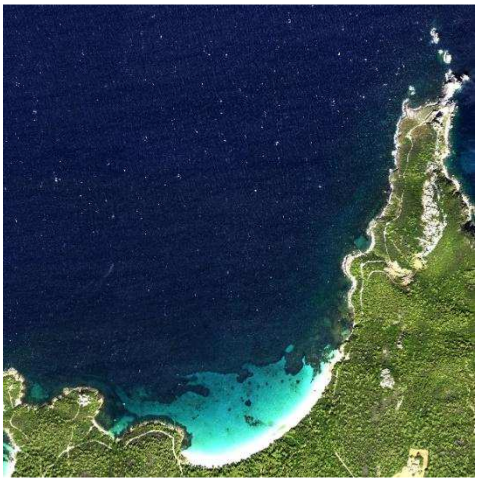

Figure 13. The true color hyperspectral image captured by HYSPEX for the Porquerolles site.

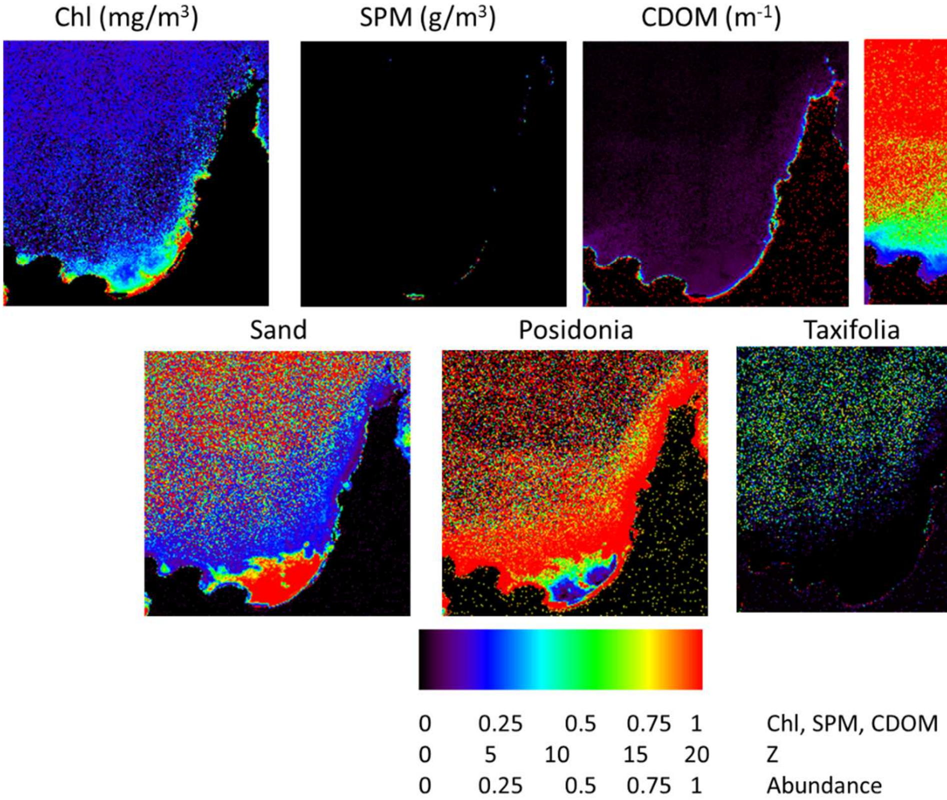

Figure 14. Estimation of water parameters (chl, SPM, CDOM), depth and seabed abundance with (#1,T,O) at Porquerolles site.

Figure 15 is an RGB image of the Toulon area with the classification map obtained with (#1,T,O).

Figure 15. Left: RGB reference image of Toulon at 2.5 m GSD. Right: Classification map with (#1,T,O).

Acknowledgements

For the estimation of leaf functional traits, we thank Susan L. Ustin (John Muir Institute of the Environment, UC Davis, CA, USA) for providing the validation dataset (NASA grant No. NNX12AP08G), NASA JPL for providing AVIRIS-NG images, and Jean-Philippe Gastellu-Etchegorry and the DART team (CESBIO) for their help in using the DART model. We also thank Marcos Herreras-Giralda (GRASP SAS) for his help with the inversion of the GRASP algorithm on synthetic data.

References

Ansalone L., Battagliere M. L., Coletta A., Facchinetti C., Fasano L., Longo F., Lopinto E., Montuori A., Pulcino V., Sacco P., Varacalli G., Zoffoli S., 2021. Hyperspectral Remote Sensing Workshop 2021: PRISMA Mission and beyond. 13-14 April 2021. https://www.asi.it/en/event/hyperspectral-remote-sensing-workshop-2021-prisma-mission-and-beyond/

Asner G. P., Martin R. E., Anderson C. B., Knapp D. E., 2015 Quantifying forest canopy traits: Imaging spectroscopy versus field survey. *Remote Sensing of Environment*, 158:15–27. https://doi.org/10.1016/j.rse.2014.11.011

Bablet A., Vu P. V. H., Jacquemoud S., Viallefont-Robinet F., Fabre S., Briottet X., Sadeghi M., Whiting M. L., Baret F., Tian J., 2018. MARMIT: A multilayer radiative transfer model of soil reflectance to estimate surface soil moisture content in the solar domain (400–2500 nm), *Remote Sensing of Environment*, 217:1–17. https://doi.org/10.1016/j.rse.2018.07.031

Berk A., Anderson G. P., Acharya P. K., Bernstein L. S., Muratov L., Lee J., Fox M., Adler-Golden S. M., Chetwynd J. H., Hoke M. L., Lockwood R. B., Gardner J. A., Cooley T. W., Borel C. C., Lewis P. E., 2005. MODTRAN 5: A reformulated atmospheric band model with auxiliary species and practical multiple scattering options: Update. Proc. SPIE 5806 Algorithms and Technologies for Multispectral, Hyperspectral, and Ultraspectral Imagery XI (Shen S.S. and Lewis P.E., eds), 1st June 2005, Orlando, FL, USA, pp. 662–667. https://doi.org/10.1117/12.606026

Briottet X., Marion R., Carrère V., Jacquemoud S., Chevrel S., Prastault P., D'Oria M., Gilouppe P., Hosford S., Lubac B., Bourguignon A., 2011. HYPXIM: A new hyperspectral sensor combining science/defence applications. In *Proc. 3rd Workshop on Hyperspectral Image and Signal Processing: Evolution in Remote Sensing (WHISPERS)*, 6-9 June 2011, Lisbon, Portugal. https://doi.org/10.1109/WHISPERS.2011.6080957

Briottet X., Asner G. P., Bajjouk T., Carrère V., Chabrillat S., et al., 2017. European hyperspectral explorer: Hypex-2. Monitoring anthropogenic influences in critical zones. *10th EARSeL SIG Imaging Spectroscopy Workshop*, April 2017, Zurich, Switzerland. 11 p. https://hal.inrae.fr/hal-02787953

Briottet X., Bajjouk T., Chami M., Delacourt C., Féret J.-B., Jacquemoud S., Minghelli A., Sheeren D., Weber C., Fabre S., Adeline K., Vaudour E., Luque S., Deville Y., Soudani K., Verpoorter C., 2022. BIODIVERSITY – A new space mission to monitor Earth ecosystem at fine scale. *Revue Française de Photogrammétrie et Télédétection*, N° 224, pp. 33-58. https://doi.org/10.52638/rfpt.2022.568

Buddenbaum H., Stern O., Paschmionka B., Hass E., Gattung T., Stoffels J., Hill J., Werner W., 2015. Using VNIR and SWIR field imaging spectroscopy for drought stress monitoring of beech seedlings. *International Journal of Remote Sensing*, 36(18):4590–4605. http://dx.doi.org/10.1080/01431161.2015.1084435

Carrère V., Briottet X., Marion R., Jacquemoud S., Bourguignon A., Chami M., Chanussot J., Chevrel S., Déliot P., Dumont M., Foucher P. Y., Minghelli-Roman A., Sheeren D., Weber C., Prastault P., Hosford S., Lefèvre-Fonollosa M. J., 2013. The French Earth observation science/defence mission HYPXIM – A second generation high spectral and spatial resolution imaging spectrometer. In *Proc. IEEE International Symposium on Geoscience and Remote Sensing*, 22-26 July 2013, Melbourne, Australia.

Cavalli R. M., Fusilli L., Pascucci S., Pignatti S., Santini F., 2008. Hyperspectral sensor data capability for retrieving complex urban land cover in comparison with multispectral data: Venice city case study (Italy). *Sensors*, 8(5):3299–3320. https://doi.org/10.3390/s8053299

Chabrillat S., Goetz A.F.G., Krosley L., Olsen H. W., 2002. Use of hyperspectral images in the identification and mapping of expansive clay soils and the role of spatial resolution. *Remote Sensing of Environment*, 82(2-3):431–445. https://doi.org/10.1016/S0034-4257(02)00060-3

Chadwick K. D., Asner G. P., 2016. Organismic-scale remote sensing of canopy foliar traits in lowland tropical forests. *Remote Sensing*, 8(2):87. https://doi.org/10.3390/rs8020087

Clark R. N., King T. V. V., Klejwa M., Swayze G. A., Vergo N., 1990. High spectral resolution reflectance spectroscopy of minerals. *Journal of Geophysical Research: Solid Earth*, 95(B8):12653–12680. https://doi.org/10.1029/JB095iB08p12653

Constans Y., Fabre S., Carfantan H., Seymour M., Crombez V., Briottet X., Deville Y., 2021. Fusion of panchromatic and hyperspectral images in the reflective domain by a combinatorial approach and application to urban landscape. In *Proc. IEEE International Geoscience and Remote Sensing Symposium*, 11-16 July 2021, Brussels, Belgium, Paper ID: 4064. https://doi.org/10.1109/IGARSS47720.2021.9554444

Davies G. E., Calvin W. M., 2017. Mapping acidic mine waste with seasonal airborne hyperspectral imagery at varying spatial scales. *Environmental Earth Sciences*. 76:432. https://doi.org/10.1007/s12665-017-6763-x

Dekker A. G., Phinn S. R., Anstee J., Bissett P., Brando V. E., Casey B., Fearns P., Hedley J., Klonowski W., Lee Z. P., Lynch M., Lyons M., Mobley C., Roelfsema C., 2011. Intercomparison of shallow water bathymetry, hydro-optics, and benthos mapping techniques in Australian and Caribbean coastal environments. *Limnology and Oceanography: Methods*, 9(9):396-425. https://doi.org/10.4319/lom.2011.9.396

Deschamps A., Marion R., Briottet X., Foucher P. Y., 2013. Simultaneous retrieval of CO_2 and aerosols in a plume from hyperspectral imagery: Application to the characterization of forest fire smoke using AVIRIS data. *International Journal of Remote Sensing*, 34(19):6837–6864. https://doi.org/10.1080/01431161.2013.809499

Dubovik O., 2004. Optimization of numerical inversion in photopolarimetric remote sensing. In *Photopolarimetry in Remote Sensing*. NATO Science Series II: Mathematics, Physics and Chemistry (Videen G., Yatskiv Y., Mishchenko M., eds), Vol 161. Springer, Dordrecht. https://doi.org/10.1007/1-4020-2368-5_3

Dubovik O., Fuertes D., Litvinov P., Lopatin A., Lapyonok T., Doubovik I., Xu F., Ducos F., Chen C., Torres B., Derimian Y., Li L., Herreras-Giralda M., Herrera M., Karol Y., Matar C., Schuster G. L., Espinosa R., Puthukkudy A., Li Z., Fischer J., Preusker R., Cuesta J., Kreuter A., Cede A., Aspetsberger M., Marth D., Bindreiter L., Hangler A., Lanzinger V., Holter C., Federspiel C., 2021. A comprehensive description of multi-term LSM for applying multiple a priori constraints in problems of atmospheric remote sensing: GRASP algorithm, concept, and applications. *Frontiers in Remote Sensing*, 2:706851. https://doi.org/10.3389/frsen.2021.706851

Dumont M., Arnaud L., Picard G., Libois Q., Lejeune Y., Nabat P., Voisin D., Morin S., 2017. In situ continuous visible and near-infrared spectroscopy of an alpine snowpack. *The Cryosphere*, 11(3):1091–1110. https://doi.org/10.5194/tc-11-1091-2017

Dupiau A., Jacquemoud S., Briottet X., Fabre S., Viallefont-Robinet F., Philpot W., Di Biagio C., Hébert M., Formenti P., 2022. MARMIT-2: An improved version of the MARMIT model to predict soil reflectance as a function of surface water content in the solar domain. *Remote Sensing of Environment*, 272:112951. https://doi.org/10.1016/j.rse.2022.112951

Dutta S., Bhattacharya B. K., Rajak D. R., Chattopadhayay C., Patel N. K., Parihar J. S., 2006. Disease detection in mustard crop using EO-1 Hyperion satellite data. *Journal of the Indian Society of Remote Sensing*, 34:325–330. https://doi.org/10.1007/BF02990661

Feingersh T., Ben Dor E., 2016. SHALOM – A commercial hyperspectral Space Mission. *Optical payloads for Space Missions*. John Wiley & Sons, Ltd, eds Shen-En Qian, https://doi.org/10.1002/9781118945179.ch11

Foucher P. Y., Déliot P., Poutier L., Duclaux O., Raffort V., Roustan Y., Temime-Roussel B., Durand A., Wortham H., 2019. Aerosol plume characterization from multitemporal hyperspectral analysis. *IEEE Journal of Selected Topics in Applied Earth Observations and Remote Sensing*, 12(7):2429–2438. https://doi.org/10.1109/JSTARS.2019.2905052

Gastellu-Etchegorry J. P., Grau E., Lauret N., 2012. DART: A 3D model for remote sensing images and radiative budget of Earth surfaces, in *Modeling and simulation in Engineering* (Alexandru C., ed.), pp. 29-68. https://doi.org/10.5772/31315

Gimenez R., Lassalle G., Elger A., Dubucq D., Credoz A., Fabre S., 2022. Mapping plant species in a former industrial site using airborne hyperspectral and time series of Sentinel-2 data sets. *Remote Sensing*, 14(15):3633. https://doi.org/10.3390/rs14153633

Gomez C., Oltra-Carrió R., Bacha S., Lagacherie P., Briottet X., 2015. Evaluating the sensitivity of clay content prediction to atmospheric effects and degradation of image spatial resolution using hyperspectral VNIR/SWIR imagery. *Remote Sensing of Environment*, 164:1–15. https://doi.org/10.1016/j.rse.2015.02.019

Gomez C., Adeline K., Bacha S., Driessen B., Gorretta N., Lagacherie P., Roger J.M., Briottet X., 2018. Sensitivity of clay content prediction to spectral configuration of VNIR/SWIR imaging data, from multispectral to hyperspectral scenarios. *Remote Sensing of Environment*, 204:18–30. https://doi.org/10.1016/j.rse.2017.10.047

Guanter L., Kaufmann H., Segl K., Foerster S., Rogass C., Chabrillat S., Kuester T., Hollstein A., Rossner G., Chlebek C., Straif C., Fischer S., Schrader S., Storch T., Heiden U., Mueller A., Bachmann M., Mühle H., Müller R., Habermeyer M., Ohndorf A., Hill J., Buddenbaum H., Hostert P., van der Linden S., Leitão P., Rabe A., Doerffer R., Krasemann H., Xi H., Mauser W., Hank T., Locherer M., Rast M., Staenz K., Sang B., 2015. The EnMAP Spaceborne Imaging Spectroscopy Mission for Earth Observation. *Remote Sensing*, 7(7):8830 –8857. https://doi.org/10.3390/rs70708830

Heinz D. C., Chang C. I., 2001. Fully constrained least squares linear spectral mixture analysis method for material quantification in hyperspectral imagery. *IEEE Transactions on Geosciences and Remote Sensing*, 39(3):529–545. http://dx.doi.org/10.1109/36.911111

Heldens W., Heiden U., Esch T., Stein E., Müller A., 2011. Can the future EnMAP mission contribute to urban applications? A literature survey. *Remote Sensing*, 3(9):1817–1846. https://doi.org/10.3390/rs3091817

Herbin H., Labonnote L. C., Dubuisson P., 2013. Multispectral information from TANSO-FTS instrument - Part 1: Application to greenhouse gases (CO_2 and CH_4) in clear sky conditions.

Atmospheric Measurement Techniques, 6(11):3301–3311, https://doi.org/10.5194/amt-6-3301-2013

Jacquemoud S., Ustin S. L., Verdebout J., Schmuck G., Andreoli G., Hosgood B., 1996. Estimating leaf biochemistry using the PROSPECT leaf optical properties model. *Remote Sensing of Environment*, 56(3):194–202. https://doi.org/10.1016/0034-4257(95)00238-3

Jia J., Chen J., Zheng X., Wang Y., Guo S., Sun H., Jiang C., Karjalainen M., Karila K., Duan Z., Wang T., Xu C., Hyyppä J., Chen Y., 2022. Tradeoffs in the spatial and spectral resolution of airborne hyperspectral imaging systems: A crop identification case study. *IEEE Transactions on Geoscience and Remote Sensing*, 60:5510918, https://doi.org/10.1109/TGRS.2021.3096999

Kruse F. A., Lefkoff A. B., Boardman J. W., Heidebrecht K. B., Shapiro A. T., Barloon P. J., Goetz A. F. H., 1993. The spectral image processing system (SIPS) - Interactive visualization and analysis of imaging spectrometer data. *Remote Sensing of Environment*, 44(2-3):145–163. https://doi.org/10.1016/0034-4257(93)90013-N

Kruse F. A., 2002. The effect of spatial resolution, spectral resolution and signal-to-noise ratio on geologic mapping using hyperspectral data, Northern data, Northern Grapevine mountains, Nevada mountains, Nevada. In *Proc. 11th JPL Airborne Earth Science Workshop*, 4-8 March 2002, Pasadena, CA, USA, 9 pp. https://aviris.jpl.nasa.gov/proceedings/workshops/00_docs/Kruse_web.pdf

Lee L. C., Liong C. Y., Jemain A. A., 2018. Partial least squares-discriminant analysis (PLS-DA) for classification of high-dimensional (HD) data: A review of contemporary practice strategies and knowledge gaps. *Analyst*, 143(15):3526-3539. https://doi.org/10.1039/c8an00599k

Lee Z., Carder K. L., Mobley C. D., Steward R. G., Patch J. S., 1999. Hyperspectral remote sensing for shallow waters: 2. Deriving bottom depths and water properties by optimization. *Applied Optics*, 38(18):3831–3843. https://doi.org/10.1364/ao.38.003831

Lennon M., Sicot G., Thomas N., Smet S., Taillandier C., Corman D., Watremez P., Gauthiez F., 2013. SWIM : un outil de cartographie de la zone de petits fonds à partir de données de télédétection optique, *Colloque Carhamb'ar, Cartographie des habitats marins benthiques : de l'acquisition à la restitution*, Brest, 26-28 mars 2013.

Lesaignoux A., Fabre S., Briottet X., 2013. Influence of soil moisture content on spectral reflectance of bare soils in the 0.4–14 μm domain. *International Journal of Remote Sensing*, 34(7):2268–2285. https://doi.org/10.1080/01431161.2012.743693

Libois Q., Picard G., France J., Arnaud L., Dumont M., Carmagnola C., King M. D., 2013. Influence of grain shape on light penetration in snow. *The Cryosphere*, 7(6):1803–1818. https://doi.org/10.5194/tc-7-1803-2013

Li L., Cheng Y. B., Ustin S. L., Hu X. T., Riaño D., 2008. Retrieval of vegetation equivalent water thickness from reflectance using genetic algorithm (GA)-partial least squares (PLS) regression. *Advances in Space Research*, 41(11):1755–1763. https://doi.org/10.1016/j.asr.2008.02.015

Litvinov P., Chen C., Dubovik O., Fuertes D., Migiletta F., Pepe M., Genesio L., Busetto L., Bindreiter L., Lanzinger V., Cobarzan P., de Graaf M., Tilstra G., Stammes P., Retsche C., 2021. New possibilities for air quality monitoring from space-borne remote sensing: Application of GRASP algorithm to S5p/TROPOMI and PRISMA measurements. *ATMOS-2021 Workshop*, ESA, 22-26 November 2021.

Liu Y. N., Sun D. X., Hu X. N., Ye X., Li Y. D., Liu S. F., Cao K. Q., Chai M. Y., Zhou W. Y. N., Zhang J., Zhang Y., Sun W. W., Jiao L. L., 2019. The Advanced Hyperspectral Imager:

Aboard China’s GaoFen-5 satellite. *IEEE Geoscience and Remote Sensing Magazine,* 7(4):23-32. https://doi.org/10.1109/MGRS.2019.2927687

Loncan L., de Almeida L. B., Bioucas-Dias J. M., Briottet X., Chanussot J., Dobigeon N., Fabre S., Liao W., Licciardi G. A., Simões M., Tourneret J. Y., Veganzone M. A., Vivone G., Wei Q., Yokoya N., 2015. Hyperspectral pansharpening: A review. *IEEE Geoscience and Remote Sensing Magazine*, 3(3):27–46. https://doi.org/10.1109/MGRS.2015.2440094

Mars J. C., Rowan L. C., 2010. Spectral assessment of new ASTER SWIR surface reflectance data products for spectroscopic mapping of rocks and minerals. *Remote Sensing of Environment*, 114(9):2011–2025. https://doi.org/10.1016/j.rse.2010.04.008

Meini M., Fossati E., Giunti L., Molina M., Formaro R., Longo F., Varacalli G., 2015. The PRISMA mission hyperspectral payload, in *Proc. 66th International Astronautical Congress*, 12-16 October 2015, Jerusalem, Israel.

Minghelli A., Vadakke-Chanat S., Chami M., Guillaume M., Peirache M., 2020. Benefit of the potential future hyperspectral satellite sensor (BIODIVERSITY) for improving the determination of water column and seabed features in coastal zones. *IEEE Journal of Selected Topics in Applied Earth Observations and Remote Sensing*, 14:1222–1232. https://doi.org/10.1109/JSTARS.2020.3031729

Miraglio T., Adeline K., Huesca M., Ustin S. L., Briottet X., 2020. Monitoring LAI, chlorophylls, and carotenoids content of a woodland savanna using hyperspectral imagery and 3D radiative transfer modeling. *Remote Sensing*, 12(1):28. https://doi.org/10.3390/rs12010028

Miraglio T., Adeline K., Huesca M., Ustin S. L., Briottet X., 2022. Assessing vegetation traits estimates accuracies from the future SBG and biodiversity hyperspectral missions over two

Mediterranean forests. *International Journal of Remote Sensing*, 43(10). https://doi.org/10.1080/01431161.2022.2093143

Nesme N., Marion R., Lezeaux O., Doz S., Camy-Peyret C., Foucher P. Y., 2021. Joint use of in-scene background radiance estimation and optimal estimation methods for quantifying methane emissions using PRISMA hyperspectral satellite data: Application to the Korpezhe industrial site. *Remote Sensing*, 13(24):4992. https://doi.org/10.3390/rs13244992

Ouerghemmi W., Le Bris A., Chehata N., Mallet C., 2017. A two-step decision fusion strategy: Application to hyperspectral and multispectral images for urban classification. *The International Archives of the Photogrammetry, Remote Sensing and Spatial Information Sciences*, XLII-1/W1:167–174. https://doi.org/10.5194/isprs-archives-XLII-1-W1-167-2017

Peyghambari S., Zhang Y., 2021. Hyperspectral remote sensing in lithological mapping, mineral exploration, and environmental geology: An updated review. *Journal of Applied Remote Sensing*, 15(3):031501. https://doi.org/10.1117/1.JRS.15.031501

Picard G., Libois Q., Arnaud L., Verin G., Dumont M., 2016. Development and calibration of an automatic spectral albedometer to estimate near-surface snow SSA time series. *The Cryosphere*, 10(3):1297–1316. https://doi.org/10.5194/tc-10-1297-2016

Poutier L., Miesch C., Lenot X., Achard V., Boucher Y., 2002. COMANCHE and COCHISE: two reciprocal atmospheric codes for hyperspectral remote sensing. In *Proc. AVIRIS Earth Sciences and Applications Workshop*, 5-8 March 2002, Pasadena, CA, USA. https://aviris.jpl.nasa.gov/proceedings/workshops/02_docs/2002_Poutier.pdf

Qian S. E., 2021. Hyperspectral satellites, evolution, and development history. *IEEE Journal of Selected Topics in Applied Earth Observations and Remote Sensing*, 14:7032–7056. https://doi.org/10.1109/JSTARS.2021.3090256

Rodgers C. D., 2000. *Inverse Methods for Atmospheric Sounding – Theory and Practice*, Series on Atmospheric Oceanic and Planetary Physics: Vol. 2, World Scientific, 256 pp. https://doi.org/10.1142/3171

Saroglu E., Bektas F., Musaoglu N., Goksel C., 2004. Fusion of multisensor remote sensing data: assessing the quality of resulting images. In *Proc. XXth ISPRS Congress Technical Commission IV* (Altan O., ed), 12-23 July 2004, Istanbul, Turkey, 5 pp. https://www.isprs.org/proceedings/XXXV/congress/comm4/papers/414.pdf

Serbin S. P., Townsend P. A., 2020. Remote sensing of plant biodiversity. Editors Cavender-Bares J., Gamon J. A., Townsend P.A. Springer Open. ISBN 978-3-030-33157-3 (eBook), https://doi.org/10.1007/978-3-030-33157-3

Sun L., Staenz K., Neville R., White H., 2006. Impact of sensor signal-to-noise ratio and spectral characteristics on hyperspectral geoscience products. In *Proc. IEEE International Symposium on Geoscience ad Remote Sensing*, 31 July 2006 – 04 August 2006, Denver, CO, USA. https://doi.org/10.1109/IGARSS.2006.534

Swayze G. A., Clark R. N., Goetz A. F. H., Chrien T. G., Gorelick N. S., 2003. Effects of spectrometer band pass, sampling, and signal-to-noise ratio on spectral identification using the Tetracorder algorithm. *Journal of Geophysical Research: Planets*, 108(E9):5105. https://doi.org/10.1029/2002JE001975

Taramelli A., Tornato A., Magliozzi M. L., Mariani S., Valentini E., Zavagli M., Costantini M., Nieke J., Adams J., Rast M., 2020. An interaction methodology to collect and assess userdriven requirements to define potential opportunities of future hyperspectral imaging Sentinel mission. *Remote Sensing*, 12(8):1286. https://doi.org/10.3390/rs12081286

Transon J., D’Andrimont R., Maugnard A., Defourny P., 2018. Survey of hyperspectral Earth observation applications from space in the Sentinel-2 context. *Remote Sensing*, 10(2):157. https://doi.org/10.3390/rs10020157

Tuzet F., Dumont M., Arnaud L., Voisin D., Lamare M., Larue F., Revuelto J., Picard G., 2019. Influence of light-absorbing particles on snow spectral irradiance profiles. *The Cryosphere*, 13(8):2169–2187. https://doi.org/10.5194/tc-13-2169-2019

Tuzet F., Dumont M., Picard G., Lamare M., Voisin D., Nabat P., Lafaysse M., Larue F., Revuelto J., Arnaud L., 2020. Quantification of the radiative impact of light-absorbing particles during two contrasted snow seasons at Col du Lautaret (2058 m a.s.l., French Alps). *The Cryosphere*, 14(12):4553–4579, https://doi.org/10.5194/tc-14-4553-2020

Ustin S. L., Middleton E. M., 2021. Current and near-term advances in Earth observation for ecological applications. *Ecological Processes*, 10:1. https://doi.org/10.1186/s13717-020-00255-4

White J. C., Coops N. C., Hilker T., Wulder M. A., Carroll A. L., 2007. Detecting mountain pine beetle red attack damage with EO-1 Hyperion moisture indices. *International Journal of Remote Sensing*, 28(10):2111–2121. https://doi.org/10.1080/01431160600944028

Yamano H., Tamura M., 2004. Detection limits of coral reef bleaching by satellite remote sensing: Simulation and data analysis. *Remote Sensing of Environment*, 90(1):86–103. https://doi.org/10.1016/j.rse.2003.12.005

Zarco-Tejada P. J., Guillén-Climent M. L., Hernández-Clemente R., Catalina A., González M. R., Martín P., 2013. Estimating leaf carotenoid content in vineyards using high resolution hyperspectral imagery acquired from an unmanned aerial vehicle (UAV). *Agricultural and Forest Meteorology*, 171–172:281–294. https://doi.org/10.1016/j.agrformet.2012.12.013

Zarco-Tejada P. J., Hornero A., Beck P. S. A., Kettenborn T., Kempeneers P., Hernandez-Clémente R., 2019. Chlorophyll content estimation in an open-canopy conifer forest with Sentinel-2A and hyperspectral imagery in the context of forest decline. *Remote Sensing of Environment*, 223:320–335. https://doi.org/10.1016/j.rse.2019.01.031

Zhao Y., Yang J., Chan J. C. W., 2014. Hyperspectral imagery super-resolution by spatial-spectral joint nonlocal similarity. *IEEE Journal of Selected Topics in Applied Earth Observations and Remote Sensing*, 7(6):2671–2679. https://doi.org/10.1109/JSTARS.2013.2292824.